

1 **Improving thermodynamic profile retrievals from microwave**
2 **radiometers by including Radio Acoustic Sounding System (RASS)**
3 **observations**

4
5
6 Irina V. Djalalova^{1,2}, David D. Turner³, Laura Bianco^{1,2},
7 James M. Wilczak², James Duncan^{1,2*}, Bianca Adler^{1,2} and Daniel Gottas²

8
9 ¹Cooperative Institute for Research in Environmental Sciences (CIRES), Boulder, CO, USA

10 ²National Oceanic and Atmospheric Administration, Physical Sciences Laboratory, Boulder, CO, USA

11 ³National Oceanic and Atmospheric Administration, Global Systems Laboratory, Boulder, CO USA

12 *Now at WindESCo, Burlington, MA

13
14
15
16
17
18 Corresponding author address: Irina V. Djalalova (Irina.V.Djalalova@noaa.gov), NOAA/Physical
19 Science Laboratory, 325 Broadway, mail stop: PSD3, Boulder, CO 80305. Tel.: 303-497-6238.
20 Fax: 303-497-6181.

| | |
|----|---------------------------------------------------------------------------------|
| 22 | Outline |
| 23 | Abstract |
| 24 | 1. Introduction |
| 25 | 2. XPIA dataset |
| 26 | 2.1 MWR measurements |
| 27 | 2.2 WPR-RASS measurements |
| 28 | 2.3 BAO data |
| 29 | 2.4 Radiosonde measurements |
| 30 | 3. Physical retrievals |
| 31 | 3.1 Iterative retrieval technique |
| 32 | 3.2 Bias-correction of MWR observations using radiosondes or climatology |
| 33 | 3.3 Analysis of physical retrieval characteristics |
| 34 | 4. Results |
| 35 | 4.1 Statistical analysis of the physical retrievals up to 3 km AGL |
| 36 | 4.2 Statistics for the profiles least close to the climatology |
| 37 | 4.3 Virtual temperature statistics |
| 38 | 5. Conclusions |
| 39 | Appendix A |
| 40 | Data availability |
| 41 | Author contribution |
| 42 | Acknowledgments |
| 43 | References |

44 **Abstract**

45 Thermodynamic profiles are often retrieved from the multi-wavelength brightness
46 temperature observations made by microwave radiometers (MWRs) using regression methods
47 (linear, quadratic approaches), artificial intelligence (neural networks), or physical-iterative
48 methods. Regression and neural network methods are tuned to mean conditions derived from
49 a climatological dataset of thermodynamic profiles collected nearby. In contrast, physical-
50 iterative retrievals use a radiative transfer model starting from a climatologically reasonable
51 profile of temperature and water vapor, with the model running iteratively until the derived
52 brightness temperatures match those observed by the MWR within a specified uncertainty.

53 In this study, a physical-iterative approach is used to retrieve temperature and humidity
54 profiles from data collected during XPIA (eXperimental Planetary boundary layer Instrument
55 Assessment), a field campaign held from March to May 2015 at NOAA's Boulder Atmospheric
56 Observatory (BAO) facility. During the campaign, several passive and active remote sensing
57 instruments as well as in-situ platforms were deployed and evaluated to determine their
58 suitability for the verification and validation of meteorological processes. Among the deployed
59 remote sensing instruments were a multi-channel MWR, as well as two radio acoustic sounding
60 systems (RASS), associated with 915-MHz and 449-MHz wind profiling radars.

61 In this study the physical-iterative approach is tested with different observational
62 inputs: first using data from surface sensors and the MWR in different configurations, and then
63 including data from the RASS into the retrieval with the MWR data. These temperature
64 retrievals are assessed against co-located radiosonde profiles. Results show that the
65 combination of the MWR and RASS observations in the retrieval allows for a more accurate

66 characterization of low-level temperature inversions, and that these retrieved temperature
67 profiles match the radiosonde observations better than the temperature profiles retrieved from
68 only the MWR in the layer between the surface and 3 km above ground level (AGL). Specifically,
69 in this layer of the atmosphere, both root mean square errors and standard deviations of the
70 difference between radiosonde and retrievals that combine MWR and RASS are improved by
71 mostly 10-20% compared to the configuration that does not include RASS observations.
72 Pearson correlation coefficients are also improved.

73 A comparison of the temperature physical retrievals to the manufacturer-provided neural
74 network retrievals is provided in Appendix A.

75

76

77

78

79

80

81

82

83

84

85

86

87

88 **1. Introduction**

89 Monitoring the state of the atmosphere for process understanding and for model
90 verification and validation requires observations from a variety of instruments, each one having
91 its set of advantages and disadvantages. Using several diverse instruments allows one to
92 monitor different aspects of the atmosphere, while combining them in an optimized synergetic
93 approach can improve the accuracy of the information available on the state of the
94 atmosphere.

95 During the eXperimental Planetary boundary layer Instrumentation Assessment (XPIA)
96 campaign, a U.S. Department of Energy sponsored experiment held at the Boulder Atmospheric
97 Observatory (BAO) in Spring 2015, several instruments were deployed (Lundquist et al., 2017)
98 with the goal of assessing their capability for measuring atmospheric boundary layer
99 meteorological variables. XPIA investigated novel measurement approaches, and quantified
100 uncertainties associated with these measurement methods. While the main interest of the XPIA
101 campaign was on wind and turbulence, measurements of other important atmospheric
102 variables were also collected, including temperature and humidity. Among the deployed
103 instruments were two identical microwave radiometers (MWRs) and two radio acoustic
104 sounding systems (RASS), as well as radiosondes launches.

105 MWRs are passive sensors, sensitive to atmospheric temperature ~~and~~ humidity ~~content~~
106 and liquid water path (LWP), that allow for a high temporal observation of the state of the
107 atmosphere, with some advantages and limitations. In order to estimate profiles of
108 temperature and humidity from the observed brightness temperatures (T_b), several methods
109 could be applied such as regressions, neural network retrievals, or physical retrieval

110 methodologies which can include additional information about the atmospheric state in the
111 retrieval process (e.g., Maahn et al. 2020). Microwave radiative transfer models (e.g.,
112 Rosenkranz, 1998; Clough et al. 2005) are commonly used to train statistical retrievals, or as
113 forward models used within physical retrieval methods. Advantages of MWRs include their
114 compact design, the relatively high temporal resolution of the measurements (2-3 minutes), the
115 possibility to observe the vertical structure of both temperature and moisture through the
116 lower part of the troposphere during both clear and cloudy conditions, and their capability to
117 operate in a standalone mode. Disadvantages include limited accuracy in the presence of rain
118 ~~because of scattering of radiation from raindrops in the atmosphere (and because water can~~
119 ~~deposit on the radome, although the instruments use a hydrophobic radome and force airflow~~
120 ~~over the surface of the radome during rain to mitigate this impact),~~ rather coarse vertical
121 resolution, and ~~for retrievals~~ the necessity to have a site-specific climatology for retrievals.
122 Other disadvantages include the challenges related to performing accurate calibrations (Küchler
123 et al., 2016, and references within), radio frequency interference (RFI), and the low accuracy on
124 the retrieved ~~liquid water path (LWP)~~ especially for values of LWP less than 20 g m^{-2} (Turner
125 2007).

126 RASS, in comparison, are active instruments that emit a longitudinal acoustic wave
127 upward, causing a local compression and rarefaction of the ambient air. These density
128 variations are tracked by the Doppler radar associated with the RASS, and the speed of the
129 propagating sound wave is measured. The speed of sound is related to the virtual temperature
130 (T_v) (North et al., 1973), and therefore, RASS are used to remotely measure vertical profiles of
131 virtual temperature in the boundary layer. Being an active instrument, the RASS is in general

132 more accurate than a passive instrument (Bianco et al., 2017), but they also come with their
133 own disadvantages. The main limitations of RASS for temperature measurements are the low
134 temporal resolution (typically a 5-min averaged RASS profile is measured once or twice per
135 hour), their limited altitude coverage, and the noise “pollution” that impacts local communities.
136 Adachi and Hashiguchi (2019) have shown that RASS could use parametric speakers to take
137 advantage of their high directivity and very low side lobes. Nevertheless, the maximum height
138 reached by the RASS ~~is still limited~~ is limited by sound attenuation, which is a function of both
139 radar frequency and atmospheric conditions (May and Wilczak, 1993) such as temperature,
140 humidity, and the advection of the propagating sound wave out of the radar’s field-of-view,
141 ~~being a function of both radar frequency and atmospheric conditions (May and Wilczak, 1993).~~
142 ~~It is determined both by the attenuation of the sound, which is a function of atmospheric~~
143 ~~temperature, humidity, and frequency of the sound source, and the advection of the~~
144 ~~propagating sound wave out of the radar’s field of view.~~ Therefore, data availability is usually
145 limited to the lowest several kilometers, depending on the frequency of the radar. In addition,
146 wintertime coverage is usually lower than that in summer, due to increased attenuation of the
147 acoustic signal in cooler and drier environments.

148 To get a better picture of the state of the temperature and moisture structure of the
149 atmosphere, it makes sense to try to combine the information obtained by both MWR and
150 RASS. Integration of different instruments has been and still is a topic of ongoing scientific
151 interest (Han and Westwater 1995; Stankov et al. 1996; Bianco et al., 2005; Engelbart et al.,
152 2009; Cimini et al., 2020; Turner and Löhnert, 2021, to name some). In this study, the focus is
153 on the combination of the MWR and RASS observations in the retrievals to improve the

154 accuracy of the temperature profiles in the lowest 3 km compared to physical retrieval
155 approaches that do not include the information from RASS measurements. Some studies have
156 used analyses from numerical weather prediction (NWP) models as an additional constraint in
157 these variational retrievals (e.g., Hewison 2007; Cimini et al. 2006, 2011; Martinet et al. 2020);
158 however, we have elected not to include model data in this study because we wanted to
159 evaluate the impact of the RASS profiles on the retrievals from a purely observational
160 perspective.

161 This paper is organized as follows: Section 2 summarizes the experimental dataset;
162 Section 3 introduces the principles of the physical retrieval approaches used to obtain vertical
163 profiles of the desired variables; Section 4 produces statistical analysis of the comparison
164 between the different retrieval approaches and radiosonde measurement; finally, conclusions
165 are presented in Section 5.

166

167 **2. XPIA dataset**

168 The data used in our analysis were collected during the XPIA experiment, held in Spring
169 2015 (March-May) at NOAA's BAO site, in Erie, Colorado (Lat.: 40.0451 N, Lon.: 105.0057 W, El.:
170 1584 m MSL). XPIA was the last experiment conducted at this facility, as after almost 40 years
171 of operations the BAO 300-m tower was demolished at the end of 2016 (Wolfe and Lataitis,
172 2018). XPIA was designed to assess the capability of different remote sensing instruments for
173 quantifying boundary layer structure, and was a preliminary study as many of these same
174 instruments were later deployed, among other campaigns, for the second Wind Forecast
175 Improvement Project WFIP2 (Shaw et al., 2019; Wilczak et al., 2019) which investigated flows in

176 complex terrain for wind energy applications, where they were for example used to study cold
177 air pools (Adler et al., 2021) and gap flow characteristics (Neiman et al., 2019; Banta et al.,
178 2020). The list of the deployed instruments included active and passive remote-sensing devices,
179 and in-situ instruments mounted on the BAO tower. Data collected during XPIA are publicly
180 available at <https://a2e.energy.gov/projects/xpia>. A detailed description of the XPIA
181 experiment can be found in Lundquist et al. (2017), while a specific look at the accuracy of the
182 instruments used in this study can be found in Bianco et al. (2017).

183

184 **2.1 MWR measurements**

185 Two identical MWRs (Radiometrics MP-3000A) managed by NOAA (MWR-NOAA) and by
186 the University of Colorado (MWR-CU), were deployed next to each other at the visitor center
187 ~600 m south of the BAO tower (see Lundquist et al., 2017 for a detailed map of the study
188 area). Prior to the experiment, both MWRs were thoroughly serviced (sensor cleaning, radome
189 replacement, etc.) and calibrated using an external liquid nitrogen target and an internal
190 ambient target. MWRs are passive devices which record the natural microwave emission in the
191 water vapor and oxygen absorption bands from the atmosphere, providing measurements of
192 the brightness temperatures. Both MWRs have 35-channels spanning a range of frequencies,
193 with 21 channels in the lower (22-30 GHz) K-band frequency band, of which 8 channels were
194 used during XPIA: 22.234, 22.5, 23.034, 23.834, 25, 26.234, 28 and 30 GHz; and 14 channels in
195 the higher (51-59 GHz) V-band frequency band, of which all were used in XPIA: 51.248, 51.76,
196 52.28, 52.804, 53.336, 53.848, 54.4, 54.94, 55.5, 56.02, 56.66, 57.288, 57.964 and 58.8 GHz.
197 Frequencies in the K-band are more sensitive to water vapor and cloud liquid water, while

198 frequencies in the V-band are sensitive to atmospheric temperature due to the absorption of
199 atmospheric oxygen (Cadeddu et al., 2013). V-band frequencies or channels can also be divided
200 in two categories: the opaque channels, 56.66 GHz and higher, that are more informative in the
201 layer of the atmosphere from the surface to ~1 km AGL, and the transparent channels, 51-56
202 GHz, that are more informative above 1 km AGL. Both MWRs observed at the zenith and at 15-
203 and 165-degree elevation angles in the north-south plane (referred to as oblique elevation
204 scans and used as their average hereafter; note zenith views have a 90-degree elevation angle).
205 However, when MWRs are deployed in locations with unobstructed views, oblique scans can be
206 performed down to 5 degrees elevation angles and may provide better temperature profile
207 accuracy in the lowest 0-1 or even 0-2 km AGL layers (Crewell and Lohnert, 2007).

208 In addition, each MWR was provided with a separate surface sensor to measure
209 pressure, temperature, and relative humidity at the installation level that was ~2.5 m AGL.
210 Vertical profiles of temperature (T), water vapor density (WVD), and relative humidity (RH)
211 were retrieved in real-time during XPIA every 2-3 minutes using a neural network (NN)
212 approach provided by the manufacturer of the radiometer (Solheim et al. 1998a, and 1998b;
213 Ware et al., 2003). Although the physical retrieval configurations used in this study do not
214 exactly match the NN retrieval configurations, a comparison of both physical and neural
215 network retrievals to the radiosonde temperature data is presented in Appendix A.

216 Both MWRs nominally operated from 9 March to 7 May 2015, although the MWR-NOAA
217 was unavailable between 5-27 April 2015. For the overlapping dates, temperature profiles
218 retrieved from the two MWRs showed very good agreement with less than 0.5 °C bias and

219 0.994 correlation (Bianco et al., 2017). For this reason, and because the MWR-CU was available
220 for a longer time period, only the MWR-CU (hereafter simply called MWR) is used.

221

222 **2.2 WPR-RASS measurements**

223 Two NOAA wind profiling radars (WPRs), operating at frequencies of 915-MHz and 449-
224 MHz, were deployed at the visitor center (same location as the MWR) during XPIA. These
225 systems are primarily designed to measure the vertical profile of the horizontal wind vector, but
226 co-located RASS also enable the observation of profiles of virtual temperature in the lower
227 atmosphere, with different resolutions and height coverages depending on the WPR. Thus, the
228 RASS associated with the 915-MHz WPR (hereafter referred to as RASS 915) measured virtual
229 temperature from 120 to 1618 m with a vertical resolution of 62 m, and the 449 MHz RASS
230 (hereafter referred to as RASS 449) sampled the boundary layer from 217 to 2001 m with a
231 vertical resolution of 105 m. The maximum height reached by the RASS is a function of both
232 radar frequency and atmospheric conditions (May and Wilczak, 1993), and is usually lower for
233 RASS 915 data, as will be shown later in the analysis.

234 The RASS data were processed using a radio frequency interference (RFI)-removal
235 algorithm (performed on the RASS spectra), a consensus algorithm (Strauch et al. 1984)
236 performed on the moment data using a 60% consensus threshold, a Weber-Wuertz outlier
237 removal algorithm (Weber et al., 1993) performed on the consensus averages, and a RASS
238 range-correction algorithm (Görsdorf and Lehmann, 2000) using an average relative humidity
239 setting of 50% determined from the available observations.

240

241 **2.3 BAO data**

242 The BAO 300-m tower was built in 1977 to study the planetary boundary layer (Kaimal
243 and Gaynor 1983). During XPIA, measurements were collected at the surface (2 m) and at six
244 higher levels (50, 100, 150, 200, 250 and 300 m AGL). Each tower level was equipped with 2
245 sonic anemometers on orthogonal booms, and one sensor based on a Sensiron SHT75 solid-
246 state sensor to measure temperature and relative humidity with a time resolution of 1 s, and
247 averaged over five minutes. The more accurate temperature and water vapor observations
248 (Horst et al., 2016) at the BAO tower 2 m AGL level are used in the physical retrieval in place of
249 the less accurate MWR ~~inline~~ surface sensor.

250

251 **2.4 Radiosonde measurements**

252 Between 9 March and 7 May 2015, while the MWR was operational, radiosondes were
253 launched by the National Center for Atmospheric Research (NCAR) assisted by several students
254 from the University of Colorado over three selected periods, one each in March, April, and May.
255 All radiosondes were Vaisala model RS92. There was a total of 59 launches, mostly four times
256 per day, around 1400, 1800, 2200, and 0200 UTC (0800, 1200, 1600 and 2000 local standard
257 time, LST). The first 35 launches, between 9-19 March, were done from the visitor center, while
258 11 launches between 15-22 April, and 13 launches between 1-4 May, were done from the
259 water tank site, ~1000 meters away from the visitor center (see Lundquist et al., 2017 for a
260 detailed map of the study area). The radiosonde measurements included temperature, dew
261 point temperature, and relative humidity to altitudes usually higher than 10 km AGL, with
262 measurements every few seconds. As a first step, for additional verification, the radiosonde

263 data from the 59 launches taken between 9 March and 4 May 2015 were compared to the BAO
264 tower measurements, up to 300 m AGL. These observed data sets match very well, with a
265 correlation coefficient of 0.99 and a standard deviation of ~ 0.7 °C. However, one radiosonde
266 profile showed a large bias (> 5 °C) against all seven levels of BAO temperature measurements
267 and all available Tv measurements from the RASS 915 (eight measurements up to 600 m AGL)
268 and from the RASS 449 (nine measurements up to 1100 m AGL), therefore this particular
269 radiosonde profile was excluded from the statistical analysis. Moreover, while accurate RASS
270 data can be collected during rain, MWR data could be potentially deteriorated due to water
271 deposition on the radome. Therefore, six profiles (three for March 13, and one each on May 1,
272 3 and 4) were eliminated from the statistical evaluation. These restrictions lowered the number
273 of total radiosonde launches used in this study to 52.

274

275 **3. Physical retrievals**

276 One way to combine the active and passive instruments would be to use the RASS
277 observations up to their maximum available height, and stitch them with the profiles obtained
278 from a physical-iterative method using MWR data. To do this, the moisture contribution to the
279 RASS virtual temperatures could be removed by using either the relative humidity measured by
280 the MWR or by a climatology of the moisture term. However, merging these different profiles
281 could result in artificial jumps at the connecting heights.

282 Alternatively, a physical retrieval (PR) iterative approach can be used to retrieve vertical
283 profiles of thermodynamic properties from the MWR and RASS observations in a synergistic
284 manner (e.g., Maahn et al 2020; Turner and Löhnert 2021). In this case, an optimal estimation-

285 based physical retrieval is initialized with a climatologically reasonable profile of temperature
286 and water vapor, and is iteratively repeated until the computed brightness temperatures match
287 those observed by the MWR within the uncertainty of the observed brightness temperatures
288 and the RASS virtual temperatures within their uncertainties (Rodgers, 2000; Turner and
289 Löhnert, 2014; [Cimini et al. 2018](#); Maahn et al. 2020).

290

291 **3.1 Iterative retrieval technique**

292 For this study, the PR uses the *TROPoe* retrieval algorithm (formerly *AERloe*, Turner and
293 Löhnert 2014; Turner and Blumberg 2019; Turner and Löhnert 2021). This algorithm is able to
294 use radiance data from microwave radiometers, infrared spectrometers, and other
295 observations as input. The microwave radiative transfer model, MonoRTM (Clough et al., 2005),
296 serves as the forward model, which is fully functional for the microwave region and was
297 intensively evaluated previously on MWR measurements (Payne et al. 2008; 2011).

298 We start with the state vector $\mathbf{X}_a = [\mathbf{T}, \mathbf{Q}, \text{LWP}]^T$, where superscript T denotes transpose,
299 and vectors and matrices are shown in bold. \mathbf{T} (K) and \mathbf{Q} (g kg^{-1}) are temperature and water
300 vapor mixing ratio profiles at 55 vertical levels from the surface up to 17 km, with the distance
301 between the levels increasing geometrically with height. LWP is the liquid water path in (g m^{-2})
302 that measures the integrated content of liquid water in the entire vertical column above the
303 MWR, and is a scalar. For this study, \mathbf{X}_a has dimensions equal to 111×1 (two vectors \mathbf{T} and \mathbf{Q}
304 with 55 levels each, and LWP). The retrieval framework of Turner and Blumberg (2019) is used,
305 but only using MWR data (no spectral infrared). Here, we demonstrate the

306 extension augmentation of the retrieval to include RASS profiles of \mathbf{Tv} , and the resulting impact
 307 this has on the retrieved temperature profiles and information content.

308 The observation vector \mathbf{Y} includes temperature and water vapor mixing ratio measured
 309 at the surface in-situ, and spectral \mathbf{Tb} measured by the MWR. The MonoRTM model \mathbf{F} is used as
 310 the forward model from the current state vector \mathbf{X} , and is then compared to the observation
 311 vector \mathbf{Y} , iterating until the difference between $\mathbf{F}(\mathbf{X})$ and \mathbf{Y} is small within a specified uncertainty
 312 (Eq 1).

313

$$X_{n+1} = X_n + (S_a^{-1} + K^T S_\epsilon^{-1} K)^{-1} K^T S_\epsilon^{-1} [Y - F(X_n) + K(X_n - X_a)] \quad (1)$$

315 with

316

$$X_a = \begin{bmatrix} T \\ Q \\ LWP \end{bmatrix} \quad S_a = \begin{bmatrix} \sigma_{TT}^2 & \sigma_{TQ}^2 & 0 \\ \sigma_{QT}^2 & \sigma_{QQ}^2 & 0 \\ 0 & 0 & \sigma_{LWP}^2 \end{bmatrix} \quad K_{ij} = \partial F_i / \partial X_j$$

317 where i and j in the K_{ij} definition mark channel and vertical level, respectively. The superscripts
 318 T and -1 in (1) indicate the transpose and inverse matrix, respectively. The observation vector \mathbf{Y}
 319 and the covariance matrix of the observed data, S_ϵ , depending on the configuration used, are
 320 equal to:

321

$$Y_1 = \begin{bmatrix} T_{sfc} \\ Q_{sfc} \\ \mathbf{Tb}_{zenith} \end{bmatrix} \quad S_{\epsilon_1} = \begin{bmatrix} \sigma_{Tsfc}^2 & 0 & 0 \\ 0 & \sigma_{Qsfc}^2 & 0 \\ 0 & 0 & \sigma_{Tb_{zenith}}^2 \end{bmatrix}$$

$$322 \quad Y_2 = \begin{bmatrix} T_{sfc} \\ Q_{sfc} \\ \mathbf{T}b_{zenith+oblique} \end{bmatrix} \quad S_{\varepsilon_2} = \begin{bmatrix} \sigma_{T_{sfc}}^2 & 0 & 0 \\ 0 & \sigma_{Q_{sfc}}^2 & 0 \\ 0 & 0 & \sigma_{\mathbf{T}b_{zenith+oblique}}^2 \end{bmatrix}$$

$$323 \quad Y_3 = \begin{bmatrix} T_{sfc} \\ Q_{sfc} \\ \mathbf{T}b_{zenith+oblique} \\ \mathbf{T}v_{RASS915} \end{bmatrix} \quad S_{\varepsilon_3} = \begin{bmatrix} \sigma_{T_{sfc}}^2 & 0 & 0 & 0 \\ 0 & \sigma_{Q_{sfc}}^2 & 0 & 0 \\ 0 & 0 & \sigma_{\mathbf{T}b_{zenith+oblique}}^2 & 0 \\ 0 & 0 & 0 & \sigma_{\mathbf{T}v_{RASS915}}^2 \end{bmatrix}$$

$$324 \quad Y_4 = \begin{bmatrix} T_{sfc} \\ Q_{sfc} \\ \mathbf{T}b_{zenith+oblique} \\ \mathbf{T}v_{RASS449} \end{bmatrix} \quad S_{\varepsilon_4} = \begin{bmatrix} \sigma_{T_{sfc}}^2 & 0 & 0 & 0 \\ 0 & \sigma_{Q_{sfc}}^2 & 0 & 0 \\ 0 & 0 & \sigma_{\mathbf{T}b_{zenith+oblique}}^2 & 0 \\ 0 & 0 & 0 & \sigma_{\mathbf{T}v_{RASS449}}^2 \end{bmatrix}$$

325 Note that the 2-m surface-level observations of temperature and water vapor mixing
 326 ratio (T_{sfc} and Q_{sfc} , respectively) are included as part of the observation vector \mathbf{Y} , and thus the
 327 uncertainties (0.5 K for temperature and less than 0.4 g kg⁻¹ for mixing ratio) in these
 328 observations are included in \mathbf{S}_ε .

329 The mean state vector of the climatological estimates, or a “prior” vector \mathbf{X}_a , is a key
 330 component in the optimal estimation framework and it is the first guess of the state vector \mathbf{X} ,
 331 \mathbf{X}_1 in Eq. (1). It provides a constraint on the ill-posed inversion problem. The prior is calculated
 332 independently for each month of the year from climatological sounding profiles (using 10 years
 333 of data) in the Denver area. The covariance matrix, \mathbf{S}_a , of the “prior” vector includes not only
 334 temperature or water vapor variances but also the covariances between them. Using around
 335 3,000 radiosondes launched by the NWS in Denver, each radiosonde profile is interpolated to
 336 the vertical levels used in the retrieval, after which the covariance of temperature and

337 temperature, temperature and humidity, and humidity and humidity is computed for different
 338 levels. LWP is arbitrarily assigned in \mathbf{X}_a , with large values chosen for its uncertainty in \mathbf{S}_a , so that
 339 it does not impact (constrain) the retrieval.

340 Four configurations are chosen for the observational vector \mathbf{Y} (\mathbf{Y}_1 , \mathbf{Y}_2 , \mathbf{Y}_3 , and \mathbf{Y}_4). In each
 341 of these, the surface observations are obtained by the 2-m BAO *in-situ* measurements of
 342 temperature and humidity. The MWR provides \mathbf{Tb} measurements from 22 channels from the
 343 zenith scan for the zenith only configuration (\mathbf{Y}_1), while when using the zenith plus oblique \mathbf{Tb}
 344 inputs (\mathbf{Y}_2 , \mathbf{Y}_3 , and \mathbf{Y}_4) the same 22 channels were used from the zenith scans together with only
 345 the four opaque channels (56.66, 57.288, 57.964 and 58.8 GHz) from the oblique scans. Using
 346 additional measurements from the co-located radar systems with RASS, the observational
 347 vector is further expanded with either RASS 915 (\mathbf{Y}_3) or RASS 449 (\mathbf{Y}_4) virtual temperature
 348 observations. The covariance matrix of the observed data, \mathbf{S}_e , depends on the chosen \mathbf{Y}_i as seen
 349 in the matrix \mathbf{S}_{ei} (with $i = 1:4$) descriptions, with increasing dimensions from \mathbf{Y}_1 to \mathbf{Y}_2 and
 350 additional increasing dimensions to \mathbf{Y}_3 or \mathbf{Y}_4 through the multi-level measurements of the RASS
 351 (Turner and Blumberg, 2019). Table 1 summarizes the observational information included in
 352 these four different configurations of the PR.

353

| | T_{sfc} | Q_{sfc} | Tb_{zenith} | $Tb_{oblique}$ | $TV_{RASS915}$ | $TV_{RASS449}$ |
|-----------------------|-----------|-----------|---------------|----------------|----------------|----------------|
| $\mathbf{Y}_1 = MWRz$ | X | X | X | | | |

| | | | | | | |
|------------------|---|---|---|---|---|---|
| $Y_2 = MWRz0$ | X | X | X | X | | |
| $Y_3 = MWRz0915$ | X | X | X | X | X | |
| $Y_4 = MWRz0449$ | X | X | X | X | | X |

354 *Table 1. Four PR configurations corresponding to the four observational Y_i vectors in Eq. (1).*

355

356 The uncertainty in the MWR Tb observations was set to the standard deviation from a
357 detrended time-series analysis for each channel during cloud-free periods. The method to
358 detect those cloud-free periods is described in detail in Section 3.2. The derived uncertainties
359 ranged from 0.3 K to 0.4 K in the 22 to 30 GHz channels, and 0.4 to 0.8 K in the 52 to 60 GHz
360 channels. We assumed that there was no correlated error between the different MWR
361 channels.

362 For the RASS, co-located RASS and radiosonde profiles were compared and the standard
363 deviation of the differences in Tv were determined as a function of the radar’s signal-to-noise
364 ratio (SNR). This relationship resulted in uncertainties that ranged from 0.8 K at high SNR values
365 to 1.5 K at low SNR values. Again, we assumed that there was no correlated error between
366 different RASS heights. Following these assumptions, the covariance matrix S_ϵ is diagonal.

367 The Jacobian matrix, K , is computed using finite differences by perturbing the elements
368 of X and rerunning the forward model. It has dimensions $m \times 111$, where m is the length of the
369 vector Y_i , therefore its dimension increases correspondingly with the inclusion of more
370 observational data. K makes the “connection” between the state vector and the observational

371 data and should be calculated at every iteration.

372

373 **3.2 Bias-correction of MWR observations using radiosondes or climatology**

374 Observational errors propagate through retrieval into the derived profiles (i.e. the bias
375 of the observed data will contribute to a bias in the retrievals). For that, retrieval uncertainties
376 in Eq. (1) from $\mathbf{Y} = \mathbf{Y}_1$ or \mathbf{Y}_2 derive only from uncertainties in surface and MWR data, while
377 retrieval uncertainties from $\mathbf{Y} = \mathbf{Y}_3$ or \mathbf{Y}_4 come from uncertainties in the surface, MWR, and RASS
378 measurements.

379 The bias of the retrieval depends on both the absolute accuracy of the forward model
380 and on any observational systematic offset, of which the systematic error in the MWR
381 observations could potentially be reduced through application of an MWR Tb bias-correction
382 procedure. In this study, two different approaches were used for the bias-correction: the first is
383 based on a comparison to the radiosondes, while the second uses climatological profiles. The
384 first method could be used for a field campaign where occasional co-located radiosonde
385 launches are taken, while the second would be used for deployments without any supporting
386 radiosonde observations.

387 For both approaches, the first step is to identify clear-sky periods during which the bias
388 can be estimated (to eliminate uncertainties associated with clouds~~to reduce the degrees of~~
389 ~~freedom associated with clouds~~) and subsequently the bias can be removed from the observed
390 MWR Tbs. One method to identify clear-sky times is to use a time-series of Tb observations in
391 the 30 GHz liquid water sensitive channel of the MWR.

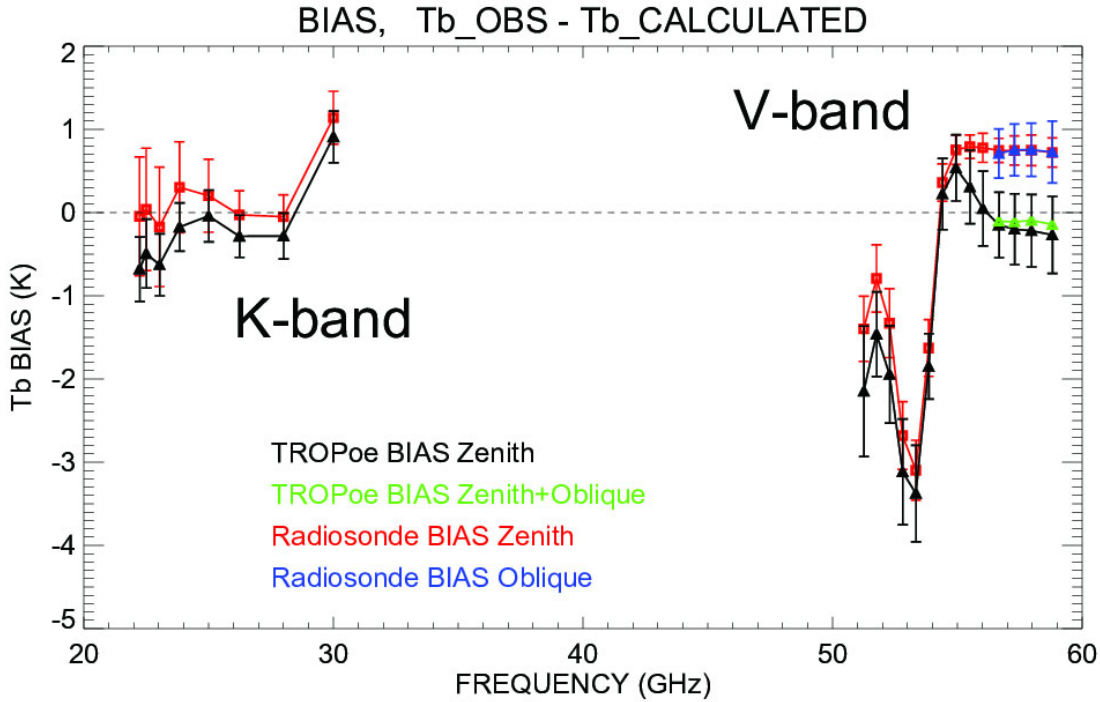
392 The standard deviation of the MWR Tb in the 30 GHz channel is calculated over a time
393 frame of one hour centered at the radiosonde launch time. The data from the zenith scan and
394 the averaged oblique scans are reviewed separately. Liquid-cloud free periods were identified
395 by cases where the temporal standard deviation was small (< 0.4 K), and more than 35
396 radiosonde profiles were classified as being launched in clear skies. The usage of the standard
397 deviation from the time-series from the oblique scans, with the same 0.4 K restriction, reduces
398 the number of the clear-sky radiosonde profiles to 18. For those chosen 18 radiosonde profiles,
399 the Tb is calculated from radiosonde temperature profiles through MonoRTM at each of the
400 MWR channels. The mean difference between these calculated radiosonde Tbs and measured
401 MWR Tbs forms the Tb bias with which the MWR Tb data can be corrected. This bias-correction
402 method will be referred to as 'radiosonde BC'.

403 While this radiosonde BC method can be employed for the XPIA dataset, for other
404 campaigns this approach would not be possible if co-located radiosonde observations were not
405 available. For this situation, an alternative method for correcting the MWR Tb biases is
406 presented. There are often spectral features in the observed minus computed brightness
407 temperature residuals that could not be explained by any physically realistic atmospheric
408 profiles, and can only result because of a calibration error in the observations. This alternative
409 bias-correction method is aimed purely to remove this unphysical spectral signature. In this
410 method, to choose clear-sky periods, the 30 GHz channel MWR Tb data are used on a daily
411 basis. The standard deviation of the MWR Tb is calculated as the average of standard deviations
412 in a one-hour sliding window through all data points of a day. Four clear-sky days were
413 identified using a threshold of 0.4 K on the standard deviation: March 10 and 30, and April 13

414 and 29, 2015. The Tb bias is then computed for each of the 22 channels as the averaged
415 difference between the observed Tb from the MWR zenith observations and the forward model
416 calculated Tbs at zenith using the TROPoe-retrieved profiles (Y_1) of those selected clear-sky
417 days. This method identified spectral calibration errors in the MWR observations that could not
418 be explained by physically realistic atmospheric profiles. This bias-correction technique, which
419 accounts for those unphysical spectral calibration features, will be referred to as 'TROPoe BC'.

420 Fig. 1 shows the Tb biases found for all 22 MWR channels from both bias-correction
421 approaches. The biases calculated with the radiosonde BC scheme are shown for all channels
422 used in our analysis: 22 channels of the zenith scan, in red, and four V-band opaque channels of
423 the oblique scans, in blue. The black and green triangles represent the biases calculated using
424 the TROPoe BC approach for zenith and for zenith+oblique scans, respectively. All biases are
425 presented with associated uncertainties (error bars representing the standard deviation over all

426 radiosondes for radiosonde BC, and mean observation Tb vector uncertainties for chosen four
 427 clear-sky days for TROPoe BC).



428 *Fig. 1. Tb biases derived from the radiosonde BC method (and TROPoe BC method) in all*
 429 *22 MWR channels of the zenith scan in red (and in black), and in the four opaque channels of*
 430 *the oblique scans in blue (and in green).*

431
 432 The biases from the two bias-correction schemes are within the uncertainties of each
 433 other for most of the channels except at the higher frequencies in the V-band. Biases in the
 434 most opaque channels are significantly affected by the accuracy of the boundary layer
 435 temperature profiles. When TROPoe BC is used, a monthly average prior temperature profile is
 436 used in the PR, and thus differences between this prior profile and the actual temperature

437 profile can result in a spectral bias in the more opaque MWR channels. On the contrary, the
438 radiosonde BC uses a direct measurement of the temperature profile (from the radiosonde),
439 and thus is more accurate. It is also important to note that, in both approaches, the biases in
440 the opaque channels for zenith and for oblique scans (for radiosonde BC these are red and blue,
441 respectively; and for the TROPoe BC these are black and green, respectively) are very similar to
442 each other. This supports the assumption that the true bias is nearly independent of the scene,
443 or that the sensitivity to the scene (e.g., zenith or off-zenith) is small.

444 The bias-correction methods were applied by removing the corresponding calculated
445 biases from the MWR Tb observations before the retrievals were performed. Later in Section 4,
446 differences in the retrieved temperature profiles will be shown when using the two bias-
447 correction approaches. These differences will be more evident in the temperature profiles
448 exhibiting near-ground temperature inversions.

449 However, the final goal of this study is not to assess the sensitivity to different bias-
450 correction approaches but to verify that the inclusion of RASS observations does improve
451 retrieved temperature profiles, independently of the bias-correction method used.

452

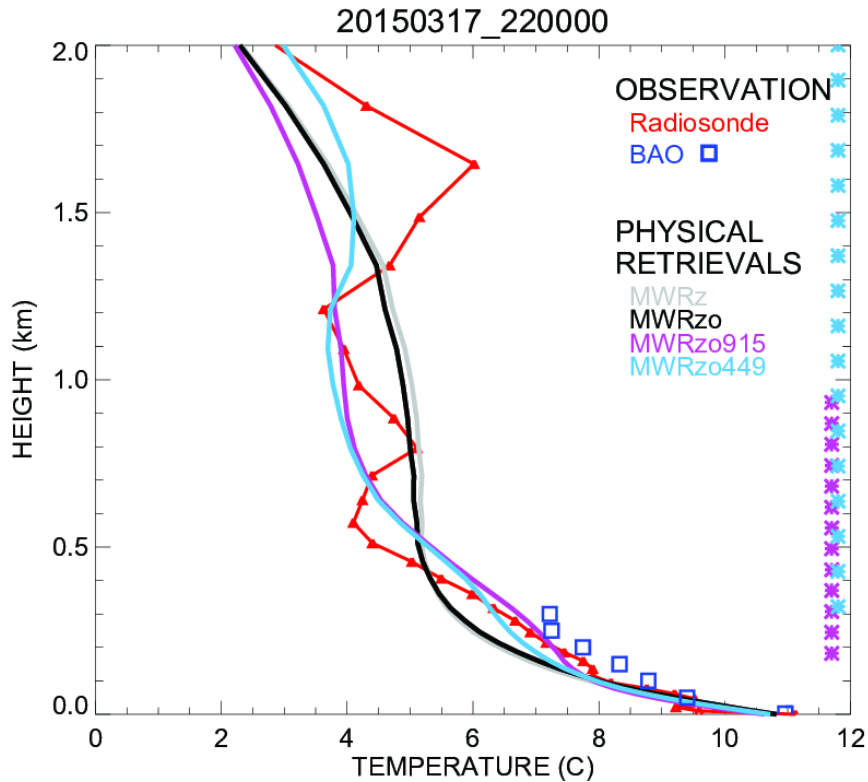
453 **3.3 Analysis of physical retrieval characteristics**

454 The retrieved profiles of the four different PR configurations presented in Table 1
455 (MWRz, MWRzo, MWRzo915, MWRzo449) were compared to the radiosonde profiles. To
456 compare radiosonde observations against the PR profiles, all radiosonde profiles were
457 interpolated vertically to the same PR heights, and PR profiles were averaged in the time
458 window between 15 minutes before and 15 minutes after each radiosonde launch. Since the

459 radiosonde ascends quite quickly in the lowest kilometers of the atmosphere (~15-20 min to
460 reach 5 km), the 30-minute temporal window is estimated to be representative of the same
461 volume of the atmosphere measured by the radiosonde. BAO tower temperature and mixing
462 ratio data at the seven available levels were used as an additional validation dataset, without
463 any vertical interpolation, averaged in the time window between 15 minutes before and 15
464 minutes after each radiosonde launch.

465 As an example of the different temperature retrievals and their relative performance,
466 data obtained on 17 March 2015 at 2200 UTC are presented in Fig. 2. Temperature profiles up
467 to 2 km AGL retrieved from the four PR configurations (MWRz, MWRzo, MWRzo915,
468 MWRzo449, using the radiosonde BC) are compared to the radiosonde data in red and to the
469 BAO measurements in blue squares. Note that all four of the PRs match the BAO observations
470 reasonably well near the ground. The MWRz and MWRzo profiles are very smooth and depart
471 quite substantially from the radiosonde measurements, being unable to reproduce the more
472 detailed structure of the atmospheric temperature profile measured by the radiosonde, while
473 the MWRzo449 profile (in light-blue) demonstrates a better agreement with both the
474 radiosonde and BAO measurements (blue squares). The MWRzo915 profile (in purple) also tries
475 to follow the elevated temperature inversion observed by the radiosonde, successfully only in
476 the lower part of the atmosphere (below 1 km AGL) where RASS 915 measurements are
477 available. This behavior will be also addressed in the following section and in the statistical
478 analysis presented later in the manuscript.

479



480

481 *Fig. 2. Temperature profiles obtained by the four PR configurations, after applying the*
 482 *radiosonde BC on the MWR Tbs: MWRz in gray, MWRzo in black, MWRzo915 in purple, and*
 483 *MWRzo449 in light-blue. These retrievals are compared to radiosonde measurements, in red,*
 484 *and BAO tower observations, in blue squares. The heights with available RASS virtual*
 485 *temperature measurements (RASS 915 in purple and RASS 449 in light-blue) are marked by the*
 486 *asterisks on the right Y-axis.*

487

488 An asset of TROPoe is that several characteristics of the PRs can be obtained from two
 489 matrices, the averaging kernel, **Akernel**, and the posterior covariance matrix, **Sop** (Masiello et
 490 al., 2012; Turner and Löhnert, 2014, Turner and Bloomberg, 2019), calculated as:

491

492
$$\mathbf{Akernel} = \mathbf{B}^{-1} \mathbf{K}^T \mathbf{S}_\varepsilon^{-1} \mathbf{K} \quad (2)$$

493 and:

494
$$\mathbf{Sop} = \mathbf{B}^{-1} \quad (3)$$

495 where:

496
$$\mathbf{B} = \mathbf{S}_a^{-1} + \mathbf{K}^T \mathbf{S}_\varepsilon^{-1} \mathbf{K}$$

497

498 All matrices, **Akernel**, **Sop**, and **B**, have dimensions 111 x 111 in our configuration. While
 499 the top left corner of the **Akernel** matrix (1:55, 1:55) is devoted to temperature, called further
 500 in the text **ATkernel**, the next (56:110, 56:110) elements are devoted to the water vapor mixing
 501 ratio, called **AQkernel**.

502 The **Akernel** provides useful information about the calculated retrievals, such as vertical
 503 resolution and degrees of freedom for signal at each level. The rows of the **Akernel** provide the
 504 smoothing functions (Rodgers, 2000) that could be applied to the radiosonde profiles (Eq. 4) to
 505 minimize the vertical representativeness error in the comparison between the various retrievals
 506 and the radiosonde profiles due to very different vertical resolutions of these profiles (Turner
 507 and Löhnert, 2014).

508 Smoothed radiosonde observed profiles can be computed using the averaging kernel,
 509 as:

510
$$\mathbf{X}_{smoothed_radiosonde} = \mathbf{Akernel} (\mathbf{X}_{radiosonde} - \mathbf{X}_a) + \mathbf{X}_a \quad (4)$$

511 The **Akernel** in Eq. (2) depends on the retrieval parameters (e.g., which datasets are
 512 used in the **Y** vector, the values assumed in the observation covariance matrix **S_ε**, and the

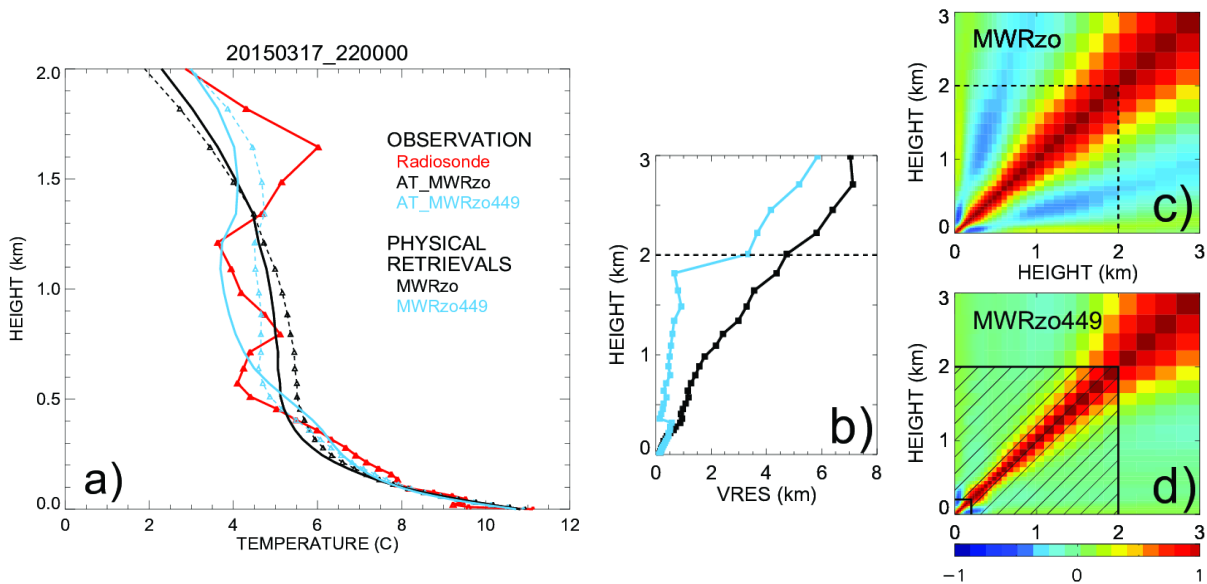
513 sensitivity of the forward model), so for our four PR configurations it is possible to calculate
514 four different kernels from Eq. (2).

515 For each of the four **Akernels**, a smoothed radiosonde profile can be computed for each
516 radiosonde profile using Eq. (4). In the presence of temperature inversions or other particular
517 structures in the atmosphere, these smoothed profiles can be quite different from each other
518 and also from the original unsmoothed radiosonde profile. Consequently, while comparison of
519 the retrievals to the relative **Akernel**-smoothed radiosonde profiles can be used to minimize the
520 vertical representativeness effects due to the different vertical resolutions of these profiles, we
521 note that a statistical comparison between the four configurations of the observational vector
522 would not be fair if each of their retrieved profiles is compared to a different **Akernel**-smoothed
523 radiosonde profile. Therefore, in the statistical analysis presented later in the manuscript
524 (section 4.2), mean bias, root mean square error (RMSE), and Pearson correlation coefficients
525 will be computed between the various TROPoe retrieval configurations and the unsmoothed
526 radiosonde profiles, just interpolated to the same vertical levels of the retrieved profiles.

527 The **ATkernel** can help understand the differences in the retrieved temperature profiles
528 obtained by the configurations using additional RASS data, shown in the example of Fig. 2.
529 Figure 3a includes the temperature profiles of the radiosonde (unsmoothed and **ATkernel**'s
530 smoothed) and PRs of MWRzo and MWRzo449 for the same example as in Fig. 2. Due to the
531 inclusion of RASS measurements, the **ATkernel**-smoothed radiosonde profile of the MWRzo449
532 configuration (dashed light-blue line) is closer to the original radiosonde data (in red) compared
533 to the black dashed profile of the MWRzo's **ATkernel**-smoothed radiosonde profile.
534 Additionally, the rows of the **ATkernel** provide a measure of the retrieval smoothing as a

535 function of altitude, so the full-width half maximum (FWHM) of each **ATkernel** row estimates
 536 the vertical resolution of the retrieved solution at each vertical level (Maddy and Barnet, 2008;
 537 Merrelli and Turner, 2012). Plots of this vertical resolution as a function of the height for the
 538 MWRzo PR and for the MWRzo449 PR are included in Fig. 3b. This plot shows that the
 539 additional observations from the RASS 449 significantly improve the vertical resolution of the
 540 retrievals.

541 The posterior covariance matrix, **Sop**, provides a measure of the uncertainty of the
 542 retrievals while the square root of the diagonal of this matrix is used to specify the 1- σ errors in
 543 the profiles of temperature or mixing ratio. Also, **Sop** shows the level-to-level dependency of
 544 the retrievals, and in an ideal case should have all non-diagonal elements equal to zero.
 545 Converted to a correlation matrix, it is possible to visualize these dependencies, as presented in
 546 Fig. 3c, d. The use of additional RASS data (MWRzo449 **Sop**, Fig. 3d) reduces the off-diagonal
 547 covariances, therefore substantially decreasing the correlations in those areas compared to the
 548 MWRzo **Sop** (Fig. 3c).



549

550 Fig. 3. a) observed temperature profiles from radiosonde, in red, from **AT** kernels smoothed
551 radiosonde, **AT_MWRzo** in dashed black, and **AT_MWRzo449** in dashed light-blue; PRs from
552 MWRzo PR in solid black, and from MWRzo449 PR in solid light-blue. b) vertical resolution
553 (VRES) as a function of the height for the MWRzo PR (black), and for the MWRzo449 PR (light-
554 blue). c) and d) 3 x 3 km (37 x 37 levels) **Sop** matrices, converted to correlation matrices, for the
555 MWRzo PR (c), and for the MWRzo449 PR (d). Dashed lines on plots b)-d) mark 2 km AGL.
556 Hatched area on panel d marks the RASS measurement heights.

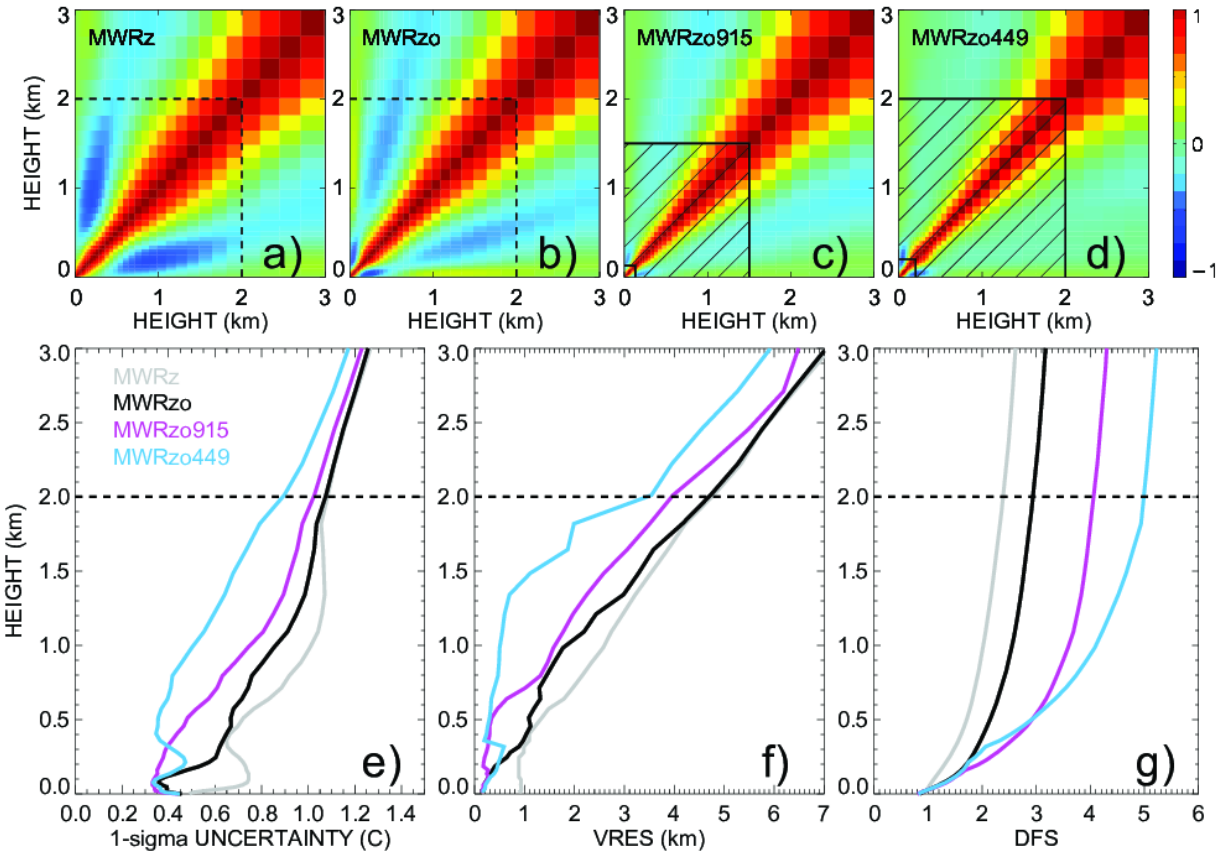
557

558 To understand the level-to-level correlations among the 4 different retrieval
559 configurations in Table 1, the **Sop** matrices were averaged over all radiosonde events, and
560 converted to correlation matrices (Fig. 4). A clearly visible narrowing of the spread around the
561 main diagonal and correlation reduction in the off-diagonal elements result by adding
562 additional observations, from MWR zenith only (Fig. 4a), to MWR zenith-oblique (Fig. 4b), to
563 the larger impact obtained by the usage of the RASS 915 (Fig. 4c), concluding with the RASS 449
564 (Fig. 4d) data. The mean retrieval uncertainty profile for each of the PR configurations is
565 presented in Fig. 4e. The uncertainty of the MWRzo449 retrieval up to 1 km AGL is around 0.5
566 °C while the other retrievals have higher uncertainties of up to 1 °C. The higher accuracy of the
567 MWRzo449 retrievals is because that configuration has more observational information
568 compared to the other retrieval configurations.

569 Other statistically important features to analyze in the PRs, besides their uncertainty,
570 are the vertical resolution already introduced in the example of Fig. 3b, and the degree of
571 freedom for signal (DFS). These two features, derived from the **A** kernels of each PR

572 configuration, averaged over all radiosonde events, are shown in Fig 4f and 4g. The vertical
573 resolution (Fig. 4f) shows the width of the atmosphere layer used for each retrieval height,
574 computed as the full-width half-maximum value of the averaging kernel. The cumulative DFS
575 profile (Fig. 4g) is a measure of the number of independent pieces of information in the
576 observations below the specified height. For example, at the 1 km AGL level the vertical
577 resolution of MWRzo449 is 0.5 km (i.e. information is from +/- 0.5 km around the retrieval
578 height is considered in the retrieval), while all other retrievals use the information from more
579 than +/- 1.5 km. Also, the DFS, as a cumulative measure, shows an increase in pieces of
580 information from MWRz to MWRzo for the whole profile and from MWRzo to MWRzo915 and
581 to MWRzo449 above ~0.2 km where RASS data are available. The DFS of MWRzo915 is higher
582 compared to the DFS of MWRzo449 in the 0.2-0.5 km AGL layer because RASS 915 data have
583 denser measurements there. It is also important to note that there is no additional information
584 added to any of the retrievals above 2km AGL, i.e. the slope of the cumulative DFS profiles are
585 equal. Despite that, the statistical analysis of the PRs up to 3 km AGL, shown in Section 4, will
586 prove that the retrieval improvements obtained by including the RASS are found even above
587 the height of the RASS measurements availability.

588



589

590 Fig. 4. Top row: The mean **Sops**, displayed as correlation matrices, for (a) MWRz, (b) MWRzo, (c)
 591 MWRzo915, and (d) MWRzo449, averaged over all radiosonde events. Hatched area on panels
 592 c) and d) marks the RASS maximum measurement heights. Bottom panels: (e) one-sigma
 593 uncertainty derived from the posterior covariance matrix in °C, (f) vertical resolution (VRES) in
 594 km, and (g) cumulative Degree of Freedom (DFS) as a function of height for temperature,
 595 averaged over all radiosonde events (MWRz is in gray, MWRzo is in black, MWRzo915 is in
 596 purple, and MWRzo449 is in light-blue). Dashed lines mark 2 km AGL on all panels.

597

598 The improvements from MWRz (in gray) to MWRzo (in black), to MWRzo915 (in purple),
 599 and finally to MWRzo449 (in light-blue) are visible in all three panels (Fig 4e-g), whereas

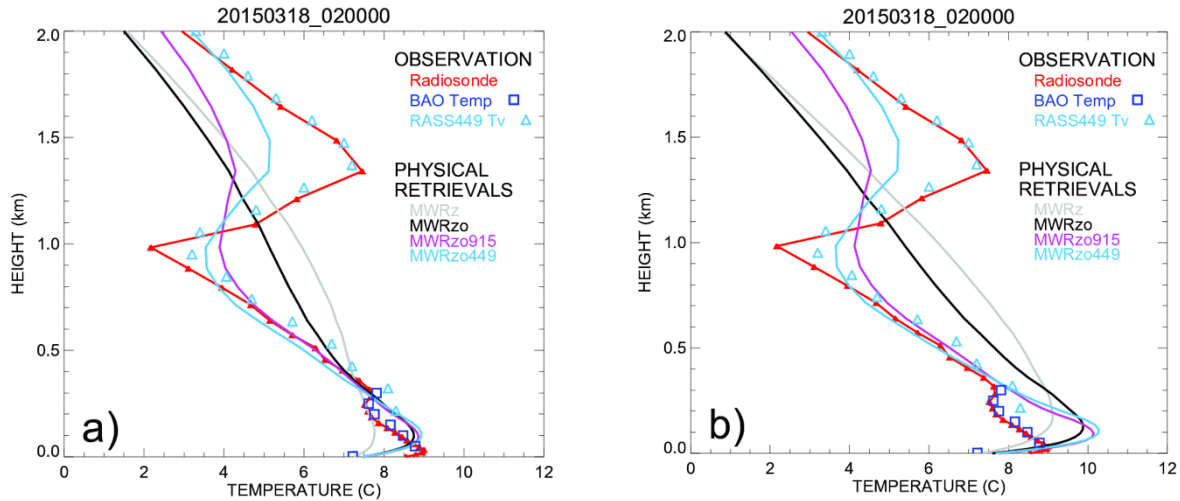
600 MWRzo449 has the lowest $1-\sigma$ uncertainty and highest DFS compared to the other PRs,
601 particularly below 2 km AGL, where RASS 449 measurements are available. Finally, it is
602 interesting that below 200 m AGL the MWRzo915 has slightly smaller lowest $1-\sigma$ uncertainty
603 and vertical resolution relative to the MWRzo449, as could be expected due to the first
604 available height of the RASS 915 being lower (120 m AGL) than the first available height for the
605 RASS 449 (217 m AGL) and due to the finer vertical resolution of the 915-MHz RASS. This
606 suggests that if additional observations were available in the lowest several 100 m of the
607 atmosphere where RASS measurements are not available, improvements might be even better
608 closer to the surface, where temperature inversions, if present, are sometimes difficult to
609 retrieve correctly.

610

611 **4. Results**

612 **4.1 Statistical analysis of physical retrievals up to 3km AGL**

613 Several cases were found during XPIA when the temperature profile exhibited
614 inversions, with the lowest happening in the surface layer. Figure 5 shows one of the most
615 complex cases, with several temperature inversions visible in the temperature profile from the
616 radiosonde (red line), in the temperature measurements from the BAO tower (blue squares),
617 and in the virtual temperature measured by the RASS 449 (light blue triangles). Note that the
618 virtual temperature profile is in close agreement with the temperature measured by
619 radiosonde.



620

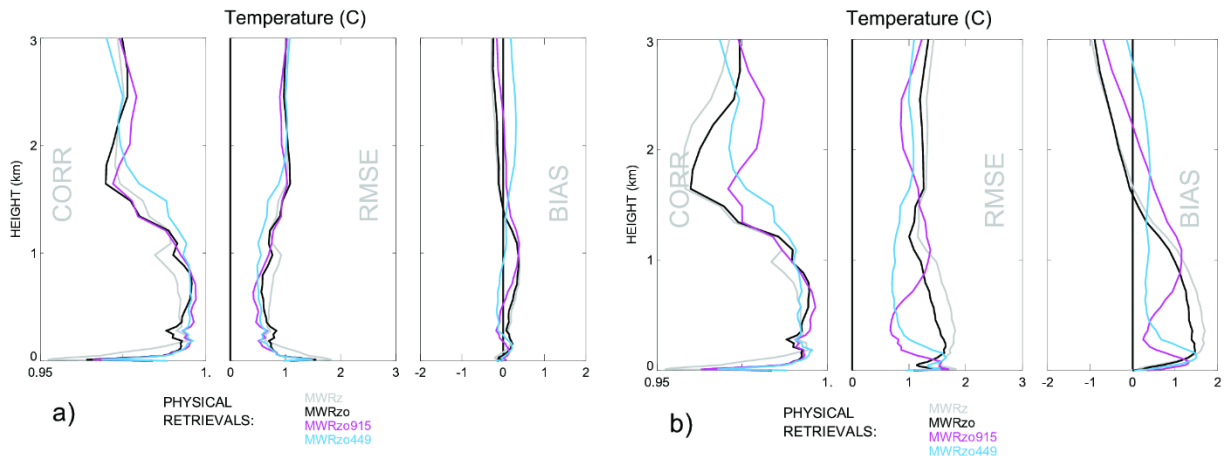
621 *Fig. 5. As in Fig. 2 but for 18 March 2015 at 0200 UTC. The RASS 449 virtual temperature is*
 622 *included as light blue triangles. a) shows the PRs obtained after applying the radiosonde BC, and*
 623 *b) shows the PRs obtained after applying the TROPoe BC on the MWR Tbs.*

624

625 Figure 5 also illustrates the difference in the temperature profiles, especially between 0-
 626 300m AGL, for the two different bias-correction schemes, which show noticeable differences in
 627 the biases of the opaque channels (especially important for the near-ground retrievals)
 628 presented in Fig. 1. As expected, the radiosonde BC method yielded a retrieved profile closer to
 629 the radiosonde temperature profile than when using TROPoe BC, for which the inversion in the
 630 temperature profile close to the surface is too accentuated (particularly the black, purple, and
 631 cyan lines, all of which used oblique scan data).

632 The relative statistical behavior (Pearson correlation, RMSE, and bias) of the PRs for
 633 both temperature and mixing ratio against radiosondes is shown in Figure 6, using both bias-
 634 correction approaches. PRs obtained after applying the radiosonde BC (Fig. 6a) present overall

635 smaller RMSE and bias (the latter almost equal to zero up to 3 km AGL) and slightly higher
 636 correlations compared to the statistics of the PRs obtained after applying the TROPoe BC (Fig.
 637 6b). This could be expected since for the comparison in Fig. 6a a subset of the radiosondes was
 638 already used for the Tb bias correction. Also, the different retrievals show a narrower
 639 distribution for the panels in Fig. 6a. Nevertheless, the results obtained when applying either
 640 bias-correction methods (in Fig. 6a, b) consistently show the improvement obtained when the
 641 RASS observations are used, with relatively smaller bias and RMSE in the 3 km layer AGL. The
 642 correlation is mainly improved above 1 km, when RASS observations are included.

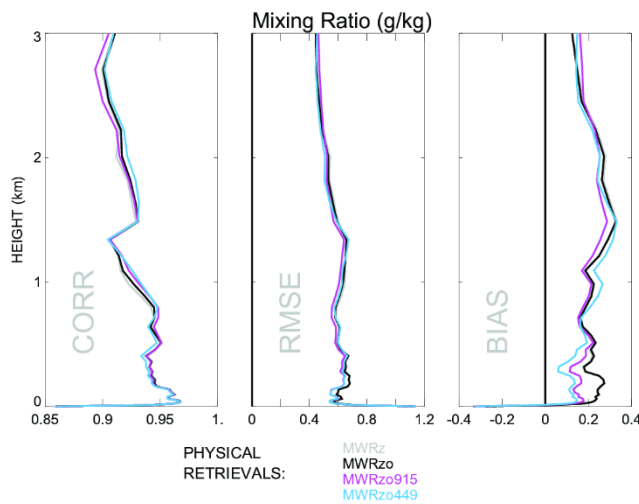


643 *Fig. 6. Pearson correlation, RMSE, and mean bias for temperature profiles of MWRz in gray,*
 644 *MWRzo in black, MWRzo915 in purple, and MWRzo449 in light-blue for the radiosonde BC bias-*
 645 *correction method in a) and TROPoe BC method in b).*

646

647 Besides temperature profiles, the PRs also provide water vapor mixing ratio profiles. It is
 648 understandable that the different configurations of PRs are not noticeably different from each
 649 other in relation to moisture, because the Tv observations from the RASS are dominated by the
 650 ambient temperature (not moisture), and thus have little impact on the water vapor retrievals.

651 We found that the **AQKernels** are almost identical for all four PR configurations (not shown).
 652 Detailed statistical evaluation of the PRs mixing ratio profiles are presented in Fig, 7, also
 653 averaged over all radiosonde events, and show very similar correlations, RMSEs, and biases for
 654 all PRs, implying that the impact of including RASS observations in the retrieval is minimal on
 655 this variable. Finally, it is noted that Fig. 7 shows the mixing ratio of the data from TROPoe BC.
 656 The radiosonde BC mixing ratio results are almost identical.



658
 659
 660
 661
 662
 663

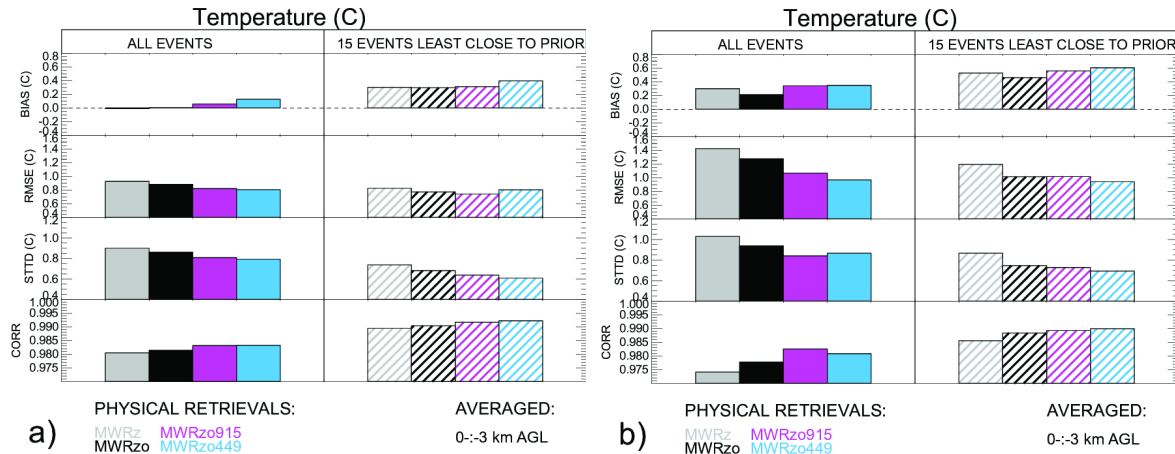
664 *Fig. 7. Same as the panels in Fig. 6b, but for mixing ratio, when using the TROPoe BC method on*
 665 *the MWR Tbs.*

666

667 **4.2 Statistics for the profiles least close to the climatology**

668 Physical retrievals use climatological data as a constraint in the retrieval. Statistically,
 669 the averaged profiles of both temperature and moisture variables are very close to the
 670 climatological averages. However, the most interesting and difficult profiles to retrieve are the
 671 cases furthest from climatology (Löhnert and Maier, 2012). To check the behavior of the
 672 retrieved data in such “extreme” cases, the RMSE was first calculated for each radiosonde

673 profile relative to the prior profiles for 37 vertical levels from the surface up to 3 km AGL, and
 674 then the 15 cases with the largest 0-3 km layer averaged RMSEs compared to the prior were
 675 selected.



676 *Fig. 8. From top to bottom: biases (retrievals minus radiosonde), RMSEs, standard deviations of*
 677 *the difference between retrievals and radiosonde, and Pearson correlations for the four PR*
 678 *configurations, averaged from the surface to 3 km AGL, and over all radiosonde data (solid*
 679 *boxes), and over the 15 extreme cases (hatched boxes). The data in panels a) use radiosonde BC,*
 680 *and in b) TROPoe BC on the MWR Tbs.*

681 Figure 8 shows the temperature statistical analysis for the entire radiosonde data set
 682 (solid boxes) and for the fifteen events far from the climatological mean (hatched boxes) for
 683 bias, RMSE, standard deviation of the differences between retrievals and radiosonde data, and
 684 Pearson correlation, calculated as the weighted averaged over the 37 vertical heights up to 3
 685 km AGL¹.

¹ The vertical grid used in the PRs is not uniform, with more frequent levels closer to the surface. If a simple average of the data from all levels is used, the near-surface layer will be weighted more compared to the upper levels of the retrievals. To avoid this, a vertical average over the lowest 3 km AGL is performed using weights at each vertical level determined by the distance between the levels.

686 Differences in the statistics when using the entire radiosonde data set or the fifteen
687 extreme profiles are noticeable for all statistical estimators. The PRs that include RASS
688 observations show better performance compared to the strictly MWR-only PR profiles (i.e.,
689 MWRz and MWRzo) for almost all statistical comparisons. This improvement is larger for the
690 PRs using the TROPoe BC (Fig. 8b) compared to the PRs using the radiosonde BC (Fig. 8a). Three
691 statistical estimators, RMSE, standard deviation, and Pearson correlation show overall better
692 values for the 15 extreme cases compared to the whole radiosonde dataset, for all PR
693 configurations and both BC approaches. This is due to the fact that for this dataset the monthly
694 averaged radiosonde profiles (for March and May particularly) depart quite substantially from
695 the monthly prior profiles. For example, the averaged radiosonde profile in March is warmer by
696 ~ 7 °C compared to the March prior (and in May by ~ 5 °C) in the first 3 km AGL. Consequently,
697 the extreme cases (mostly found in March) have the warmest radiosonde temperature profiles,
698 but are overall closer to the monthly averaged radiosonde profiles.

699 Table 2 includes the same data as in Figure 8 but as a percentage of the improvement,
700 compared to the MWRz retrievals.

701

702

703

704

705

706

| 0-3 km AGL | ALL EVENTS | | | | | 15 EVENTS LEAST CLOSE TO THE PRIOR | | | |
|----------------------------|------------|-------|------------------|------------------|--|---------------------------------------|-------|------------------|------------------|
| RADIOSONDE BIAS-CORRECTION | | | | | | | | | |
| | MWRz | MWRzo | MWRzo RASS915 | MWRzo RASS449 | | MWRz | MWRzo | MWRzo RASS915 | MWRzo RASS449 |
| RMSE | 0% | 5% | 11% | 13% | | 0% | 7% | 10% | 3% |
| STTD | 0% | 4% | 10% | 12% | | 0% | 8% | 14% | 17% |
| CORR | 0% | 0.1% | 0.3% | 0.3% | | 0% | 0.1% | 0.2% | 0.3% |
| TROPoe BIAS-CORRECTION | | | | | | | | | |
| RMSE | 0% | 10% | 25% | 32% | | 0% | 15% | 15% | 21% |
| STTD | 0% | 9% | 18% | 16% | | 0% | 14% | 16% | 20% |
| CORR | 0% | 0.4% | 0.9% | 0.7% | | 0% | 0.3% | 0.4% | 0.4% |

707

708 *Table 2. Retrieval improvements for different RASS/MWR configurations as a percentage*

709 *compared to MWRz.*

710

711 The results presented in Table 2 show improvements in all statistical estimations when
712 including RASS observations, with improvements in RMSE between 10 and 20 %, demonstrating
713 the positive impact derived by the inclusion of the active measurements, regardless of the bias-
714 correction method used, but larger for the TROPoe BC data because there is more room for
715 improvement when this BC method is used. Improvements in the Pearson correlation

716 coefficients are small because correlation, determined during XPIA by the overall temperature
717 structure with height and diurnal cycle, is already good, leaving little room for improvement.

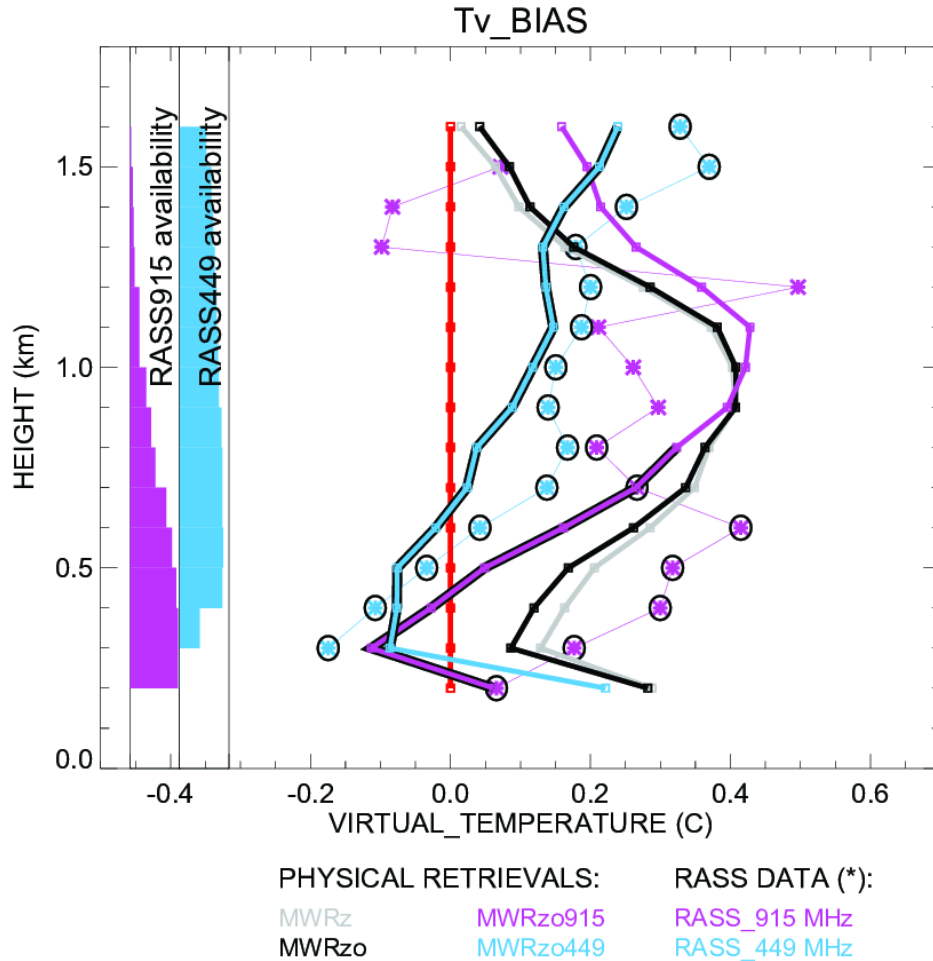
718

719 **4.3 Virtual temperature profile statistics**

720 Using the physical retrieval outputs, “retrieved virtual temperature profiles” can also be
721 calculated. In this section the direct comparison of these retrieved virtual temperature profiles
722 and RASS virtual temperature profiles to the original radiosonde is shown. With this comparison
723 we want to show how the biases of the retrieved profiles relate to the original RASS Tv biases.

724 Figure 9 shows Tv retrieved profile biases compared to the original radiosonde data ~~as~~
725 ~~solid lines,~~ and ~~These Tv profiles and~~ RASS 915 and RASS 449 Tv bias ~~as asterisks.~~ RASS data are
726 interpolated on a regular vertical grid, going from 200 m to 1.6 km with a 100 m
727 range resolution, for easy comparison.

728 ~~A zero bias is denoted by the red line. On the left side of the figure the bar charts of the~~
729 ~~RASS measurement availability are shown as a function of height. The widest part of these~~
730 ~~charts corresponds to 100% data availability. Heights with RASS availability greater than 50%~~
731 ~~are marked with additional circles over the asterisks.~~



732

733 *Fig. 9. Bias of virtual temperature for all PR configurations compared to the original radiosonde*
 734 *measurements. A zero bias is denoted by the red line. RASS data biases are marked by asterisks*
 735 *and by additional circles for the RASS data with more than 50% availability, according to the*
 736 *availability bar charts on the left.*

737 *All PRs profiles are derived after applying the radiosonde BC method.*

738

739 While RASS 449 data are available at almost all heights up to 1.6 km, the RASS 915 data
 740 availability decreases considerably with height, lowering to 50% availability around 800 m AGL.

741 The PRs that include RASS data, MWRzo915 and MWRzo449, are also marked with additional
742 black lines at the heights with at least 50% of relative RASS data availability. In agreement with
743 Fig. 6a, this figure clearly shows the superiority of the MWRzo449 and MWRzo915 (in the layer
744 with > 50% RASS data availability) compared to the MWRz and MWRzo configurations, which
745 do not include RASS data. For MWRzo449, RASS 449 data were almost always available,
746 therefore it is easy to identify a similarity between the Tv bias profiles of the RASS 449 and the
747 PRs including it. Thus, for the MWRzo449 the Tv bias is more uniform through the heights
748 compared to all other PRs that do not include RASS data. Moreover, it is noted a roughly
749 constant offset between the MWRzo449 Tv and RASS 449 Tv biases profiles, with their
750 averaged difference equal to ~ 0.08 °C (when the radiosonde BC is used), and to ~ 0.32 °C (when
751 the TROPoe BC is used, not shown), over the ~ 1.3 km (0.3-1.6 km) atmospheric layer where
752 more than 50% of the RASS 449 measurements are available, uniformly distributed through the
753 heights. The inclusion of the RASS into the PRs does reduce the values of the biases in the
754 retrievals even below the values of the RASS biases, because of the combined information from
755 RASS and MWR.

756

757 5. Conclusions

758 In this study, data collected during the XPIA field campaign were used to test different
759 configurations of a physical-iterative retrieval (PR) approach in the determination of
760 temperature and humidity profiles from data collected by microwave radiometers, surface
761 sensors, and RASS measurements. The accuracy of several PR configurations was tested: two
762 configurations made use only of surface observations and MWR observed brightness

763 temperature (zenith only, MWRz; and zenith plus oblique, MWRzo); while two others included
764 the active virtual temperature profile observations available from co-located RASS (one, RASS
765 915, associated with a 915-MHz; and the other, RASS 449, associated with a 449-MHz wind
766 profiling radar). Radiosonde launches were used for verification of the retrieved profiles. In
767 Appendix A, the performance of MWRz and MWRzo retrieved profiles and Neural Network
768 retrieved profiles against the radiosondes was evaluated.

769 To remove any observational systematic error in the MWR Tb observations, two bias-
770 correction procedures were tested. The first one takes advantage of the many radiosondes
771 launched during XPIA, and the second one uses climatological profiles. As expected, the
772 radiosonde bias-correction method gives retrieved profiles closer to the radiosonde
773 temperature profiles than when using the climatological based method. Nevertheless, our
774 results show that regardless of the bias-correction method used, the inclusion of the
775 observations from the active RASS instruments in the PR approach improves the accuracy of the
776 temperature profiles by around 10-20% compared to the PR configuration using only surface
777 observations and MWR observed brightness temperature from the zenith scan. Of the PRs
778 configurations tested, generally better statistical agreement is found with the radiosonde
779 observations when the RASS 449 is used together with the surface observations and brightness
780 temperature from the zenith and averaged oblique MWR observations.

781 The **AKernel** and the posterior covariance matrices for temperature are used to derive
782 the one-sigma uncertainty, vertical resolution, and cumulative degree of freedom as a function
783 of height for the different PRs, and the level-to-level correlated uncertainty of the retrievals.
784 Results show that the inclusion of the active instruments improves all of the above-mentioned

785 variables in the 0-3km layer, including at heights between 2-3km that are above the maximum
786 RASS height. Thus, the positive impact of the RASS observations extends into the atmosphere
787 above the height of measurements themselves.

788 Furthermore, 15 cases when temperature profiles from the radiosonde observations
789 were the furthest away from the mean climatological average were selected, and the statistical
790 comparison was reproduced over this subset of cases. These are the cases usually the most
791 difficult to retrieve and the most important to forecast; therefore, it is essential to improve the
792 retrievals in these situations. Even for this subset of selected cases the inclusion of active
793 sensor observations in the PRs is found to be beneficial.

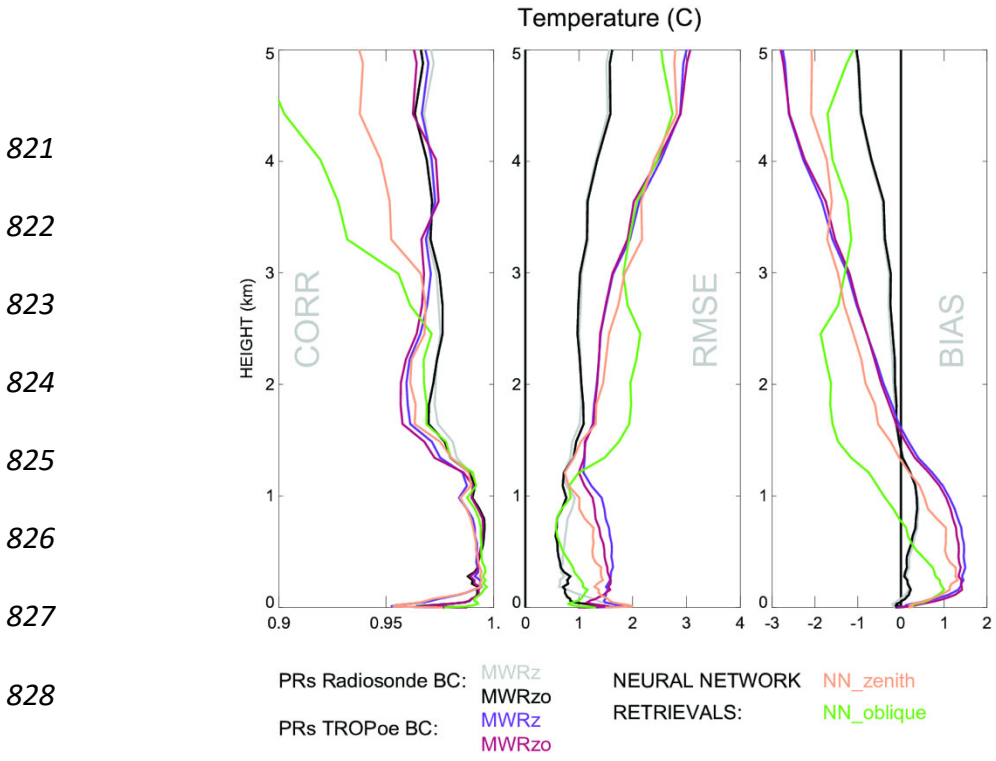
794 Finally, the impact of the inclusion of RASS measurements on the retrieved humidity
795 profiles was considered, but the inclusion of RASS observations did not produce significantly
796 better results, compared to the configurations that do not include them. This was not a surprise
797 as RASS measures virtual temperature, effectively adding very little extra information to the
798 water vapor retrieval. In this case a better option would be to consider adding other active
799 remote sensors such as water vapor differential absorption lidars (DIALs) to the PRs. Turner and
800 Löhnert (2021) showed that including the partial profile of water vapor observed by the DIAL
801 substantially increases the information content in the combined water vapor retrievals.
802 Consequently, to improve both temperature and humidity retrievals a synergy between MWR,
803 RASS, and DIAL systems would likely be necessary.

804

805 **Appendix A**

806 The neural network (NN) retrievals developed by the vendor explicitly for XPIA use a
807 training dataset based on a 5-year climatology of profiles from radiosondes launched at the
808 Denver International Airport, 35 miles south-east from the XPIA site. NN-based MWR vertical
809 retrieval profiles were obtained using the zenith or an average of two oblique elevation scans,
810 15- and 165-degrees (not including the zenith), all with 58 levels extending from the surface up
811 to 10 km, with nominal vertical grid depending on the height (every 50 m from the surface to
812 500 m, every 100 m from 500 m to 2 km, and every 250 m from 2 to 10 km, AGL).

813 Fig. 1A shows composite NN vertical profiles of temperature (separately for the zenith
814 and averaged obliques) calculated for radiosonde launch times, and the corresponding PR
815 profiles already introduced in Fig. 6a, b. For a proper comparison, only MWRz and MWRzo
816 profiles are used, without including RASS measurements. It has to be noted that since the “NN
817 oblique” retrieval provided by the manufacturer of the radiometer does not include the zenith,
818 this configuration cannot be considered exactly equivalent to the MWRzo PR.



821
822
823
824
825
826
827

828
829

830 *Fig. 1A. Pearson correlation, RMSE, and mean bias for temperature profiles for MWRz in grey*
 831 *(and purple) and MWRzo in black (and maroon) when the radiosonde BC (and the TROPoe BC)*
 832 *method is applied. Included in this figure are the NN temperature profiles, from the zenith scan*
 833 *(in beige), and from the averaged oblique scans (in green).*

834

835 Another difference to point out is that, while the MWR Tb data have been bias-
 836 corrected before being used in the PR configurations, as discussed in Section 3.2, the NN
 837 retrievals use the uncorrected Tb, since it was non-trivial to reprocess those retrievals. Martinet
 838 et al. (2015) showed that when it is possible to bias-correct the MWR Tb before applying the
 839 NN retrieval technique, the NN retrievals are not impacted below 1 km AGL, but a clear
 840 improvement of NN retrievals in terms of RMSE and bias are observed between 1 and 3 km

841 altitude. As is visible in Fig. 1A, this is the layer of the atmosphere where the NN profiles (beige
842 and green lines) have larger bias and RMSE, compared to the PR profiles.

843 When the radiosonde BC method is used, the MWRz and MWRzo PRs (gray and black
844 lines) present better statistics through the entire profiles shown in Fig. 1A, with larger values of
845 the correlation coefficient, and smaller values of RMSE and bias. The oblique only NN profiles
846 (in green) show comparable statistics to the PRs employing the radiosonde BC method up to 1
847 km AGL, with degraded performances above this height. Above 1 km AGL, the zenith NN
848 profiles (in beige) do better than the oblique NN in terms of RMSE and bias. When the TROPoe
849 BC method is used, the MWRz and MWRzo PRs (purple and maroon lines) perform better than
850 the NN profiles only in terms of RMSE and bias, and only between 1.5 and 3 km AGL ~~and above~~
851 ~~around 1.5 km AGL.~~

852 The better performance obtained by the MWRz and MWRzo PRs that use the
853 radiosonde BC approach demonstrate the importance of having an accurate and reliable
854 method for bias correcting the MWR.

855

856 **Data availability**

857 All data are publicly accessible at the DOE Atmosphere to Electrons Data Archive and
858 Portal, found at <https://a2e.energy.gov/projects/xpia> (Lundquist et al., 2016).

859

860 **Author contribution**

861 Irina Djalalova completed the primary analysis using the XPIA dataset. Daniel Gotta
862 contributed to the post-processing of the RASS data. Dave Turner modified the TROPoe

863 algorithm to include the RASS data as input. All authors contributed to the analysis of the
864 results. Irina Djalalova prepared the manuscript with contributions from all co-authors.

865

866 **Acknowledgements**

867 We thank all the people involved in XPIA for instrument deployment and maintenance,
868 data collection, and data quality control, and particularly the University of Colorado Boulder for
869 making the CU MWR data available. We are very grateful for the constructive comments and
870 suggestions provided by the two anonymous Referees and by the Editor, which we believe have
871 greatly improved the clarity of the manuscript. Funding for this study was provided by the
872 NOAA/ESRL Atmospheric Science for Renewable Energy (ASRE) program.

873

874 **Competing interests** The authors declare no competing interests.

875

876 **References**

877 Adachi, A. and H. Hashiguchi: Application of parametric speakers to radio acoustic sounding
878 system. **ATMOS MEAS TECH**, **12**, 5699–5715, [https://doi.org/10.5194/amt-12-5699-](https://doi.org/10.5194/amt-12-5699-2019)

879 [2019](https://doi.org/10.5194/amt-12-5699-2019), 2019.

880 Adler, B., J. M. Wilczak, L. Bianco, I. Djalalova, J. B. Duncan Jr., D. D. Turner: Observational case
881 study of a persistent cold air pool and gap flow in the Columbia River Basin. **J APPL**

882 **METEOROL CLIM**, **60**, 1071-1090, <https://doi.org/10.1175/JAMC-D-21-0013.1>, 2021.

883 Banta, R. M., and coauthors: Characterizing NWP model errors using Doppler lidar

884 measurements of recurrent regional diurnal flows: Marine-air intrusions into the

885 Columbia River Basin. **MON WEATHER REV**, **148**, 927-953,
886 <https://doi.org/10.1175/MWR-D-19-0188.1>, 2020.

887 Bianco L., D. Cimini, F. S. Marzano, and R. Ware: Combining microwave radiometer and wind
888 profiler radar measurements for high-resolution atmospheric humidity profiling, **J**
889 **ATMOS OCEAN TECH**, **22**, 949–965, <https://doi.org/10.1175/JTECH1771.1>, 2005.

890 Bianco, L., K. Friedrich, J. M. Wilczak, D. Hazen, D. Wolfe, R. Delgado, S. Oncley, and J. K.
891 Lundquist: Assessing the accuracy of microwave radiometers and radio acoustic
892 sounding systems for wind energy applications. **ATMOS MEAS TECH**, **10**, 1707-1721,
893 <https://doi.org/10.5194/amt-10-1707-2017>, 2017.

894 Cadeddu, M. P., J. C. Liljegren, and D. D. Turner: The Atmospheric radiation measurement
895 (ARM) program network of microwave radiometers: instrumentation, data, and
896 retrievals, **ATMOS MEAS TECH**, **6**, 2359–2372, [https://doi.org/10.5194/amt-6-2359-](https://doi.org/10.5194/amt-6-2359-2013)
897 [2013](https://doi.org/10.5194/amt-6-2359-2013), 2013.

898 Cimini, D., T. J. Hewison, L. Martin, J. Guldner, C. Gaffard, F. S. Marzano: Temperature and
899 humidity profile retrievals from ground-based microwave radiometers during TUC,
900 **METEOROL Z**, Vol. 15, No. 5, 45-56, [DOI: 10.1127/09411-D-2948/2006/0099](https://doi.org/10.1127/09411-D-2948/2006/0099), 2006.

901 Cimini, D., E. Campos, R. Ware, S. Albers, G. Giuliani, J. Oreamuno, P. Joe, S. E. Koch, S. Cober,
902 and E. Westwater: Thermodynamic Atmospheric Profiling during the 2010 Winter
903 Olympics Using Ground-based Microwave Radiometry, **IEEE T GEOSCI REMOTE**, **49**, 12,
904 <https://doi.org/10.1109/TGRS.2011.2154337>, 2011.

905 Cimini, D., Rosenkranz, P. W., Tretyakov, M. Y., Koshelev, M. A., and Romano, F.: Uncertainty of
906 atmospheric microwave absorption model: impact on ground-based radiometer

907 simulations and retrievals, **ATMOS CHEM PHYS**, **18**, 15231–15259,
908 <https://acp.copernicus.org/articles/18/15231/2018>, 2018.

909 Cimini, D., M. Haeffelin, S. Kotthaus, U. Löhnert, P. Martinet, E. O'Connor, C. Walden, M.
910 Collaud Coen, and J. Preissler: Towards the profiling of the atmospheric boundary layer
911 at European scale—introducing the COST Action PROBE. **Bulletin of Atmospheric
912 Science and Technology**, **1**, 23–42, <https://doi.org/10.1007/s42865-020-00003-8>, 2020.

913 Clough, S.A., M. W. Shephard, E. J. Mlawer, J. S. Delamere, M. Iacono, K. E. Cady-Pereira, S.
914 Boukabara and P. D. Brown: Atmospheric radiative transfer modeling: A summary of the
915 AER codes, **J QUANT SPECTROSC RA**, vol 91, no. 2, pp 233-244,
916 <https://doi.org/10.1016/j.jqsrt.2004.05.058>, 2005.

917 Crewell, S., U. Löhnert: Accuracy of Boundary Layer Temperature Profiles Retrieved With
918 Multifrequency Multiangle Microwave Radiometry, **IEEE T GEOSCI REMOTE**, VOL. 45,
919 NO. 7, JULY 2007, [DOI: 10.1109/TGRS.2006.888434](https://doi.org/10.1109/TGRS.2006.888434), 2007.

920 Engelbart, D., W. Monna, J. Nash: Integrated Ground-Based Remote-Sensing Stations for
921 Atmospheric Profiling, **COST Action 720 Final Report**, EUR 24172,
922 <https://doi.org/10.2831/10752>, 2009.

923 Görsdorf, U., and V. Lehmann: Enhanced Accuracy of RASS-Measured Temperatures Due to an
924 Improved Range Correction. **J ATMOS OCEAN TECH**, **17 (4)**, 406–416,
925 [https://doi.org/10.1175/1520-0426\(2000\)017<0406:EAORMT>2.0.CO;2](https://doi.org/10.1175/1520-0426(2000)017<0406:EAORMT>2.0.CO;2), 2000.

926 Han, Y., and E. R. Westwater: Remote sensing of tropospheric water vapor and cloud liquid
927 water by integrated ground-based sensors. **J ATMOS OCEAN TECH**, **12**, 1050-1059, DOI:
928 [https://doi.org/10.1175/1520-0426\(1995\)012<1050:RSOTWV>2.0.CO;2](https://doi.org/10.1175/1520-0426(1995)012<1050:RSOTWV>2.0.CO;2), 1995.

929 Hewison, T.: 1D-VAR Retrieval of Temperature and Humidity Profiles From a Ground-Based
930 Microwave Radiometer, **IEEE T GEOSCI REMOTE**, **45(7)**, 2163–2168,
931 <https://doi.org/10.1109/TGRS.2007.898091>, 2007.

932 Horst, T. W., S. R. Semmer, and I. Bogoev: Evaluation of Mechanically-Aspirated
933 Temperature/Relative Humidity Radiation Shields, 18th Symposium on Meteorological
934 Observation and Instrumentation, AMS Annual Meeting, New Orleans, LA, 10-15
935 January 2016, <https://ams.confex.com/ams/96Annual/webprogram/Paper286839.html>,
936 2016.

937 Kaimal, J. C., and J. E. Gaynor: The Boulder Atmospheric Observatory. **J CLIM APPL METEOROL**,
938 **22**, 863–880, [https://doi.org/10.1175/1520-0450\(1983\)022<0863:TBAO>2.0.CO;2](https://doi.org/10.1175/1520-0450(1983)022<0863:TBAO>2.0.CO;2), 1983.

939 Kuchler, N., D. D. Turner, U. Lohnert, and S. Crewell: Calibrating ground-based microwave
940 radiometers: Uncertainty and drifts, **RADIO SCI**, **51**, 311–327,
941 [doi:10.1002/2015RS005826](https://doi.org/10.1002/2015RS005826), 2016.

942 Lohnert U. and O. Maier: Operational profiling of temperature using ground-based microwave
943 radiometry at Payerne: prospects and challenges. **ATMOS MEAS TECH**, **5**, 1121–1134,
944 <https://doi.org/10.5194/amt-5-1121-2012>, 2012.

945 Lundquist, J. K., J. M. Wilczak, R. Ashton, L. Bianco, W. A. Brewer, A. Choukulkar, A. Clifton, M.
946 Debnath, R. Delgado, K. Friedrich, S. Gunter, A. Hamidi, G. V. Iungo, A. Kaushik, B.
947 Kosović, P. Langan, A. Lass, E. Lavin, J. C.-Y. Lee, K. L. McCaffrey, R. K. Newsom, D. C.
948 Noone, S. P. Oncley, P. T. Quelet, S. P. Sandberg, J. L. Schroeder, W. J. Shaw, L. Sparling,
949 C. St. Martin, A. St. Pe, E. Strobach, K. Tay, B. J. Vanderwende, A. Weickmann, D. Wolfe,
950 and R. Worsnop: Assessing state-of-the-art capabilities for probing the atmospheric

951 boundary layer: the XPIA field campaign. **B AM METEOROL SOC**, **98**, 289–314,
952 <https://doi.org/10.1175/BAMS-D-15-00151.1>, 2017.

953 Maahn, M., D. D. Turner, U. Löhnert, D. J. Posselt, K. Ebell, G. G. Mace, and J. M. Comstock:
954 Optimal estimation retrievals and their uncertainties: What every atmospheric scientist
955 should know. **B AM METEOROL SOC**, **101**, E1512-E1523, [https://doi.org/10.1175/BAMS-](https://doi.org/10.1175/BAMS-D-19-0027.1)
956 [D-19-0027.1](https://doi.org/10.1175/BAMS-D-19-0027.1), 2020.

957 Maddy, E. S. and C. D. Barnet: Vertical Resolution Estimates in Version 5 of AIRS Operational
958 Retrievals. **IEEE T GEOSCI REMOTE**, VOL. **46**, NO. 8, AUGUST 2008,
959 <https://doi.org/10.1109/TGRS.2008.917498>, 2008.

960 Martinet, P., A. Dabas, J.-M. Donier, T. Douffet, O. Garrouste, and R. Guillot: 1D-Var
961 temperature retrievals from microwave radiometer and convective scale model, **TELLUS**
962 **A**, **67:1**, <https://doi.org/10.3402/tellusa.v67.27925>, 2015.

963 Martinet, P., D. Cimini, F. Burnet, B. Ménétrier, Y. Michel, and V. Unger: Improvement of
964 numerical weather prediction model analysis during fog conditions through the
965 assimilation of ground-based microwave radiometer observations: a 1D-Var study,
966 **ATMOS MEAS TECH**, **13**, 6593–6611, <https://doi.org/10.5194/amt-13-6593-2020>, 2020.

967 May, P. T. and J. M. Wilczak: Diurnal and Seasonal Variations of Boundary-Layer Structure
968 Observed with a Radar Wind Profiler and RASS. **MON WEATHER REV**, **121**, 673–682,
969 [https://doi.org/10.1175/1520-0493\(1993\)121<0673:DASVOB>2.0.CO;2](https://doi.org/10.1175/1520-0493(1993)121<0673:DASVOB>2.0.CO;2), 1993.

970 Masiello, G., C. Serio, and P. Antonelli: Inversion for atmospheric thermodynamical parameters
971 of IASI data in the principal components space. **Q J ROY METEOR SOC**, **138**, 103–117,
972 <https://doi.org/10.1002/qj.909>, 2012.

973 Merrelli, A. M., and D. D. Turner: Comparing information content of upwelling far infrared and
974 midinfrared radiance spectra for clear atmosphere profiling. **J ATMOS OCEAN TECH**, **29**,
975 510–526, <https://doi.org/10.1175/JTECH-D-11-00113.1>, 2012.

976 Neiman, P. J., D. J. Gottas, and A. B. White: A Two-Cool-Season Wind Profiler–Based Analysis of
977 Westward-Directed Gap Flow through the Columbia River Gorge. **MON WEATHER REV**,
978 **147**, 4653-4680, <https://doi.org/10.1175/MWR-D-19-0026.1>, 2019.

979 North, E. M., A. M. Peterson, and H. D. Parry: RASS, a remote sensing system for measuring low-
980 level temperature profiles. **B AM METEOROL SOC**, **54**, 912–919, 1973.

981 Payne, V. H., J. S. Delamere, K. E. Cady-Pereira, R. R. Gamache, J.-L. Moncet, E. J. Mlawer, and S.
982 A. Clough: Air-broadened half-widths of the 22- and 183-GHz water-vapor lines. **IEEE T**
983 **GEOSCI REMOTE**, **46**, 3601-3617, <https://doi.org/10.1109/TGRS.2008.2002435>, 2008.

984 Payne, V. H., E. J. Mlawer, K. E. Cady-Pereira, and J.-L. Moncet: Water vapor continuum
985 absorption in the microwave. **IEEE T GEOSCI REMOTE**, **49**, 2194-2208,
986 <https://doi.org/10.1109/TGRS.2010.2091416>, 2011.

987 Rodgers, C. D.: Inverse Methods for Atmospheric Sounding: Theory and Practice. Series on
988 Atmospheric, Oceanic and Planetary Physics, Vol. 2, World Scientific, 238 pp, 2000.

989 Rosenkranz, P. W.: Water vapour microwave continuum absorption: A comparison of
990 measurements and models. **RADIO SCI**, **33**, 919–928,
991 <https://doi.org/10.1029/98RS01182>, 1998.

992 Shaw, W., and Coauthors: The Second Wind Forecast Improvement Project (WFIP 2): General
993 Overview. **B AM METEOROL SOC**, **100(9)**, 1687–1699, [https://doi.org/10.1175/BAMS-D-](https://doi.org/10.1175/BAMS-D-18-0036.1)
994 [18-0036.1](https://doi.org/10.1175/BAMS-D-18-0036.1), 2019.

995 Solheim, F., J. R. Godwin, J., and R. Ware: Passive ground-based remote sensing of atmospheric
996 temperature, water vapor, and cloud liquid profiles by a frequency synthesized
997 microwave radiometer. **METEOROL Z**, **7**, 370–376, 1998a.

998 Solheim F., J. R. Godwin, E. R. Westwater, Y. Han, S. J. Keihm, K. Marsh, R. Ware: Radiometric
999 profiling of temperature, water vapor and cloud liquid water using various inversion
1000 methods. **RADIO SCI**, **33**, 393–404, <https://doi.org/10.1029/97RS03656>, 1998b.

1001 Stankov, B. B., E. R. Westwater, and E. E. Gossard: Use of wind profiler estimates of significant
1002 moisture gradients to improve humidity profile retrieval. **J ATMOS OCEAN TECH**, **13**,
1003 1285-1290, DOI:
1004 [https://doi.org/10.1175/15200426\(1996\)013<1285:UOWPEO>2.0.CO;2](https://doi.org/10.1175/15200426(1996)013<1285:UOWPEO>2.0.CO;2), 1996.

1005 Strauch, R. G., D. A. Merritt, K. P. Moran, K. B. Earnshaw, and D. V. De Kamp: The Colorado
1006 wind-profiling network. **J ATMOS OCEAN TECH**, **1**, 37–49, [https://doi.org/10.1175/1520-
1007 0426\(1984\)001<0037:tcwpm>2.0.co;2](https://doi.org/10.1175/1520-0426(1984)001<0037:tcwpm>2.0.co;2), 1984.

1008 Turner, D. D.: Improved ground-based liquid water path retrievals using a combined infrared
1009 and microwave approach. **J GEOPHYS RES-ATMOS**, **112**, D15204,
1010 <https://doi.org/10.1029/2007JD008530>, 2007.

1011 Turner, D. D., and U. Löhnert: Information content and uncertainties in thermodynamic profiles
1012 and liquid cloud properties retrieved from the ground-based Atmospheric Emitted
1013 Radiance Interferometer (AERI). **J APPL METEOROL CLIM**, **53**, 752–771,
1014 <https://doi.org/10.1175/JAMC-D-13-0126.1>, 2014.

1015 Turner, D. D., and W. G. Blumberg: Improvements to the AERlloe thermodynamic profile
1016 retrieval algorithm. **IEEE J-STARS**, **12(5)**, 1339–1354,
1017 <https://doi.org/10.1109/JSTARS.2018.2874968>, 2019.

1018 Turner, D. D., and U. Löhnert: Ground-based Temperature and Humidity Profiling: Combining
1019 Active and Passive Remote Sensors. **ATMOS MEAS TECH**, **14**, 3033–3048,
1020 <https://doi.org/10.5194/amt-2020-352>, 2021.

1021 Ware R., Solheim F., Carpenter R., and Coauthors: A multi-channel radiometric profiler of
1022 temperature, humidity and cloud liquid. **RADIO SCI**, **38**, No. 4, 8079,
1023 <https://doi.org/10.1029/2002RS002856>, 2003.

1024 Weber, B. L., D. B. Wuertz, D. C. Welsh, and R. Mcpeek: Quality controls for profiler
1025 measurements of winds and RASS temperatures. **J ATMOS OCEAN TECH**, **10**, 452–464,
1026 [https://doi.org/10.1175/1520-0426\(1993\)010<0452:gcfpmo>2.0.co;2](https://doi.org/10.1175/1520-0426(1993)010<0452:gcfpmo>2.0.co;2), 1993.

1027 Wilczak, J. M., and Coauthors: The Second Wind Forecast Improvement Project (WFIP2):
1028 Observational Field Campaign. **B AM METEOROL SOC**, **100(9)**, 1701–1723,
1029 <https://doi.org/10.1175/BAMS-D-18-0035.1>, 2019.

1030 Wolfe, D. E. and R. J. Lataitis: Boulder Atmospheric Observatory: 1977–2016: The end of an era
1031 and lessons learned. **B AM METEOROL SOC**, **99**, 1345–1358,
1032 <https://doi.org/10.1175/BAMS-D-17-0054.1>, 2018.

1033